# Fan Noise Predictions of the NASA Source Diagnostic Test using Unsteady Simulations with LAVA Part II - Tonal and Broadband Noise Assessment

Luis S. Fernandes\*, Jeffrey A. Housman<sup>†</sup>, Gerrit-Daniel Stich<sup>‡</sup> and Jared C. Duensing<sup>§</sup> NASA Ames Research Center, M/S 258-2, Moffett Field, California, 94035

The NASA Source Diagnostic Test (SDT) campaign experimental data is used for validation of a sliding mesh technique recently implemented within the Launch, Ascent, and Vehicle Aerodynamics computational framework for time-accurate simulation of rotating fans. The far-field acoustics are analyzed in this work, building upon the aerodynamic validation studies previously published in Part I. Two modeling approaches are explored: the unsteady Reynoldsaveraged Navier Stokes (uRANS) with the negative Spalart-Allmaras (SA-neg) turbulence model closure, and a hybrid Reynolds-averaged Navier Stokes/large-eddy simulation (RANS/LES) paradigm employing a zonal detached-eddy simulation (ZDES) closure with enhanced shielding protection. Two convective flux scheme approaches with different dissipation properties are also explored with ZDES. The Ffowcs-Williams and Hawkings (FW-H) permeable surface approach is used for propagation of the near-field acoustics to the far-field microphone locations. This work analyzes the low-speed (approach) condition, characterized by a fan rotation speed of 7808 rotations-per-minute (RPM). Three different grid levels ranging between 200 million and 1.1 billion grid points are considered. Results show good prediction of the broadband noise levels at sideline angles ranging between 70° and 110°. The forward arc observers show an underprediction of the overall sound pressure levels (OASPL) even at the fine grid level. A breakdown of the inlet and exhaust contributions reveals a steep drop-off in the broadband noise levels past a blade-passing frequency (BPF) of 1.5, potentially caused by a lack of resolved small-scale turbulent fluctuations in the interstage region. Past 110° the OASPL are over-predicted by up to 10 dB due to an over-prediction of the low-frequency broadband noise levels in the aft arc. The detuning of BPF<sub>2</sub> caused by small deviations in the blade stagger angle around the wheel is captured, and a corresponding decrease in the sound power level for this cut-on tone is observed.

## I. Introduction

The current trend in turbofan development is increasingly focused on higher bypass ratios, which come with an associated increase in the fan diameter. This architecture provides an increase in the turbofan efficiency, and is characterized by lower fan rotational speeds and reduced jet exhaust velocities. These Ultra-High Bypass Ratio (UHBR) turbofan engines promise a reduction in noise levels and increased efficiency, offering a near-term solution to the ever-increasing demands of urban air traffic and FAA regulations.

However, the increase in the fan size for these UHBR turbofan architectures presents important challenges that cannot be overlooked during design. For instance, fan noise is projected to become the dominant noise source at both take-off and approach conditions (Envia, 2002a). Specifically, the interaction of the fan blade wakes and the downstream outlet-guide vanes (OGVs), commonly referred to as rotor-stator interaction, has been identified as the dominant mechanism responsible for fan noise (Peake and Parry, 2012). This mechanism is well-understood, and is known to generate both tonal and broadband noise, as follows. The interstage flow-field can be thought of as the sum of two components in a frame of reference rotating with the fan: a steady flow containing the mean blade wakes, which are identical and periodic in the azimuthal direction, and an unsteady flow corresponding to the fluctuating components of the turbulent blade wakes. Tonal noise is generated by the repeated interaction of the mean blade wakes with the

<sup>\*</sup>Research Scientist, Science and Technology Corporation, Computational Aerosciences Branch, AIAA Member, luismsfern@nasa.gov

<sup>†</sup>Research Scientist, Computational Aerosciences Branch, AIAA Senior Member, jeffrey.a.housman@nasa.gov

<sup>\*</sup>Research Scientist, Science and Technology Corporation, Computational Aerosciences Branch, AIAA Member, gerrit-daniel.stich@nasa.gov

<sup>§</sup>Computational Aerosciences Branch Chief, Computational Aerosciences Branch, AIAA Member, jared.c.duensing@nasa.gov

rigid OGVs positioned downstream, at frequencies corresponding to multiples of the blade-passing frequency (BPF)  $B\Omega$ , where  $\Omega$  is the fan rotation speed and B is the number of fan blades. On the other hand, the interaction of the turbulent fluctuating flow-field with the OGVs gives rise to a broadband noise spectrum in the stationary frame. As a result, computational methods that solve for the mean flow-field, e.g. Reynolds-Averaged Navier-Stokes (RANS), are only able to capture the tonal noise resulting from this mechanism.

Despite the importance of rotor-stator interaction noise, other noise sources from even the simplest model turbofan may be identified. Fan self-noise, produced primarily by the transfer of momentum from the fan blades to the surrounding fluid, is responsible for both tonal and broadband noise. The tonal noise component arises from the steady flow in the rotating frame around the fan blades, which produces acoustic tones at harmonics of the BPF ( $B\Omega$ ). Some of the acoustic modes corresponding to the BPF tones are cut-off according to the Tyler and Sofrin selection rule (Tyler and Sofrin, 1962), as long as blade-tip speeds remain subsonic; but as the fan speed increases and the blade tip becomes supersonic, these modes transition to a cut-on state and can propagate into the far-field (Peake and Parry, 2012). Additionally, the generation of broadband rotor self-noise can be attributed to the interaction between the trailing edge and the turbulent boundary layer forming over the suction side of each blade. The interaction of the fan blade tips with the turbulent boundary layer developing over the rotor casing is another broadband noise generating mechanism that is challenging to model, and occurs despite the high flight Reynolds numbers, where even the thinner boundary layers associated with this regime are disrupted by each blade pass due to the small blade tip clearances usually on the order of tenths of a millimeter.

A vital consideration of simulating the noise signature of these fan configurations lies in the general assumption that the fan blades are uniformly distributed in the circumferential direction. This is often not the case, and small stagger angle deviations may be present due to installation effects around the wheel, leading to a redistribution of the energy contained in the BPF tones into multiple pure tones (MPTs), or sub-BPF harmonics - so-called buzz-saw noise. This is especially noticeable at supersonic blade tip speeds, where shock waves form in the outboard region of the fan blades near the leading edge. Due to their nonlinear character, these shock waves are extremely sensitive to small variations in the blade-to-blade stagger angles, which leads to the generation of lower-strength tones across all shaft orders, instead of collapsing into a common BPF harmonic. Although the presence of MPTs is more pronounced at transonic/supersonic blade tip speeds through the fan self-noise mechanism just described, subsonic blade tip speeds may also show MPTs as a result of slight differences in the individual rotor-stator interactions due to blade-to-blade deviations in the stagger angle. The acoustic energy that would otherwise be associated with the BPF harmonics in an idealized fan with uniformly spaced blades can thus bleed into shaft-order tones even at subsonic blade tip speeds, typical of approach conditions.

Targeted noise reduction technologies have become widespread over the long history of turbofan engine development. The Tyler & Sofrin selection rule links the harmonics of the tonal noise to duct modes that are cut-off (evanescent) by clever selection of the number of fan and OGV blade counts. This technique is primarily used to prevent the propagation of the first BPF across the forward arc. Addition of acoustic liners in the nacelle inlet and exhaust are also effective means to target the dampening of forward- and aft-propagating tonal modes. Yet, while effective techniques exist to control the tonal noise propagation resulting from the rotor-stator interaction, mitigating the propagation of the broadband noise remains a challenge. The imbalance in our understanding of broadband noise generation mechanisms, accentuated by the lack of effectiveness of current turbofan acoustic dampening techniques targeting broadband noise, together with the imminent need for UHBR turbofan engines to help meet engine efficiency demands, indicates both an interest and a necessity to broaden our understanding in this field. The capability to employ computational fluid dynamics (CFD) tools for modeling the aeroacoustics environment around these complex systems is therefore invaluable, particularly in its capacity to analyze various configurations swiftly compared to experimental testing. Development of this toolset is therefore vital for the guidance of future noise reduction technologies.

An important component of developing this toolset is validation. NASA conducted an extensive aircraft noise reduction effort through the Advanced Subsonic Technology (AST) program in the mid-1990s (Envia, 2002a). Several experimental tests were performed as part of the AST program, many of which had the goal of identifying and characterizing the main noise generation mechanisms within a turbofan engine. An experimental campaign that resulted from this program was the NASA Source Diagnostic Test (SDT), conducted at the NASA John H. Glenn Research Center 9×15 ft. Low Speed Anechoic Wind Tunnel (LSWT). Photos of the experimental installation are shown in Fig. 1. Extensive analysis and discussion of the results gathered in the test are available in Podboy et al. (2002a); Hughes et al. (2002); Hughes (2002); Heidelberg (2002); Premo and Joppa (2002); Woodward et al. (2002); Envia (2002b); Podboy et al. (2002b). This comprehensive dataset is used in the present work as a validation test case for the Launch, Ascent and Vehicle Aerodynamics (LAVA) solver framework in the context of fan noise generation and far-field propagation, particularly when it comes to the accuracy provided by simulating the fan rotation using a recently-implemented sliding

mesh technique.







- (a) Rotor-alone configuration frontal view.
- (b) Rotor-alone configuration side view.
- (c) Full configuration frontal view.

Fig. 1 SDT fan model installed in the NASA John H. Glenn Research Center  $9 \times 15$  ft. Low Speed Anechoic Wind Tunnel (LSWT). Rotor-alone configuration (left and center) - not considered in this work - and full configuration with nacelle (right) studied in the present work. Image courtesy of Hughes (2002).

Several research groups have attempted to model the SDT model turbofan in the past decade with varying degrees of success. Shur et al. (2018); Suzuki et al. (2018, 2019) have published a set of studies analyzing the aerodynamic and aeroacoustic fields generated by the SDT. They used unsteady RANS (uRANS) and a hybrid zonal RANS/large-eddy simulation (LES) combined with a volume synthetic turbulence generator (VSTG) to inject turbulent content downstream of the fan blades. The lattice Boltzmann code PowerFLOW has also been utilized with a very large-eddy simulation model (VLES) to simulate the subsonic approach condition initially (Casalino et al., 2018), as well as the transonic take-off condition more recently (Gonzalez-Martino and Casalino, 2018). Notably, the authors report an improvement in the noise predictions when explicit tripping of the rotor blade suction side flow is employed. Attempts at using LES to simulate the SDT case have also been explored. Pérez Arroyo et al. (2019) used an explicit LES approach to solve a circumferentially-periodic version of the geometry (with one less OGV blade from the actual model turbofan). The study achieves good agreement in the high-frequency broadband noise levels, but shows an over-prediction of the low-frequency content attributed to the presence of oversized coherent turbulent structures in the rotor tip gap region. Hah and Romeo (2017) employed a similar geometric modification to study the rotor wake development while avoiding the large computational costs associated with simulating the full 360° domain. The differences in the interstage flow-field predicted by uRANS and LES are highlighted in the study. One of the key insights developed from examining these studies was that scale-resolving simulations that faired well in terms of the far-field noise levels predicted (primarily at low-frequencies) were distinguished by the presence of artificial turbulence generation mechanisms, either via the addition of source-terms downstream of the blades, or through tripping of the blade suction side surface flow. This observation emphasizes the importance of capturing the interstage flow-field, in particular the decay of the fan blade wakes into small-scale turbulence prior to their interaction with the OGV blades.

For the reasons highlighted thus far, RANS-based methods should be able to model the tonal component of the acoustic mechanisms described, but fail to capture the broadband component resulting from the interaction of the unsteady turbulent flow-field with the surrounding geometry. In this work, the tone-capturing capability of unsteady RANS is evaluated and contrasted with a scale-resolving hybrid RANS/LES approach with a zonal detached-eddy simulation (ZDES) closure employing an enhanced protection of attached boundary layers (Deck and Renard, 2020). This study builds upon the aerodynamic validation studies performed in Fernandes et al. (2023), and aims to cover the aeroacoustic validation efforts in the context of the recently-implemented sliding mesh technique within the LAVA solver. To that end, far-field acoustics are estimated using the permeable surface integral method of Ffowcs-Williams and Hawkings (FW-H) (di Francescantonio, 1997) in a frequency-domain formulation (Lockard, 2002).

A description of the test setup is provided in Sec. II, followed by a brief overview of the computational methods (Sec. III) utilized in this work. A discussion of the results obtained with uRANS and hybrid RANS/LES is provided in Sec. IV. This section is broken-down into a near-field flow analysis (Sec. IV.A) and a far-field acoustic analysis (Sec. IV.B). The latter will include several sensitivity studies and a grid refinement study conducted for the low-speed regime. Finally, the effect of introducing asymmetries to the nominal blade stagger angle is analyzed in Sec. IV.C. Concluding remarks are then summarized in Sec. V.

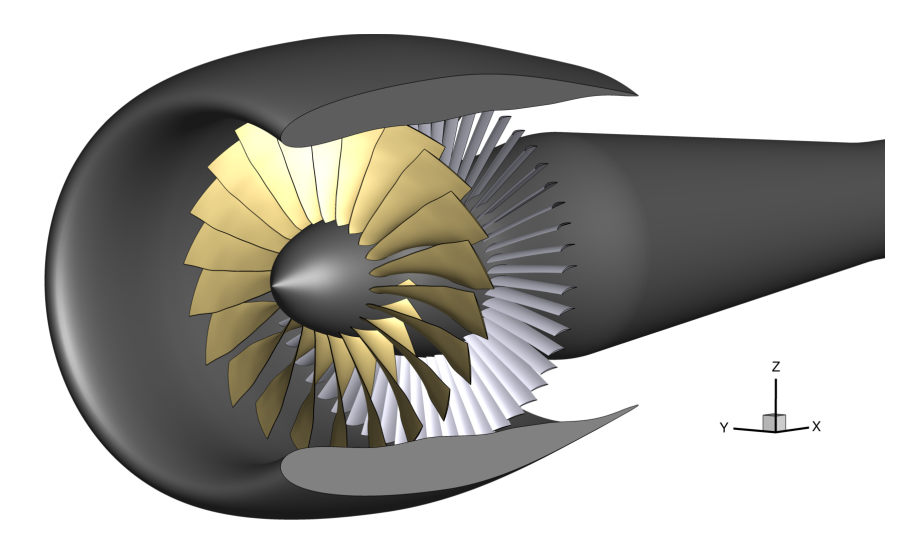


Fig. 2 Overview of SDT geometry with R4 fan and baseline OGV installed.

## II. Turbofan Model and Setup Description

Several versions of a model turbofan underwent testing during the NASA Source Diagnostic Test experimental campaign. The present study focuses on the primary test rotor, designated R4, composed of a 22-inch (0.5572 m) diameter ( $D_f$ ) fan and is made up of 22 identical blades. Three different outlet-guide-vane (OGV) designs were assessed in the experiment, with this work focusing on the baseline OGV featuring 54 unswept, equally-spaced blades. Importantly, none of the tested variants included a core flow, instead representing the secondary stream present in modern turbofan engines. A spinner is linked to the centerbody strut support arm, which was secured to the wind tunnel floor in the experimental test rig. A perspective view of the geometry is presented in Fig. 2. The experiment included five different fan rotational speeds, ranging from 7808 rotations-per-minute (RPM), or 61.7 % of the design speed, to 12,657 RPM (100 % of the design speed). This study will focus on the low-speed (7808 RPM) approach condition. The high-speed transonic condition corresponding to 12,657 RPM is currently being analyzed, and results for this regime will be published in the future. These speed settings represent significantly different flow-field conditions, aiming to assess the capabilities and limitations of the LAVA solver framework at both subsonic and transonic blade tip speeds - the fan tip Mach number for these two conditions varies between 0.6694 and 1.085, based on the freestream speed of sound.

The freestream is representative of take-off and landing conditions, characterized by sea-level pressure and temperature and a Mach number of  $M_{\infty}=0.1$ . An extensive dataset suitable for validation of computational models was collected during the experiment. Single-point hot-wire probe measurements at two different axial stations in the interstage region allow characterization of the rotor wake flow-field (Podboy et al., 2002a). Laser Doppler velocimetry (LDV) velocity measurements at different survey locations are also available (Podboy et al., 2002a,b) for quantification of the wake flow, blade tip flow and shock location in the fan stage (high-speed case only). Aerodynamic fan stage performance results are compiled in Hughes et al. (2002); Hughes (2002) for both a rotor-alone nacelle (RAN) system and the complete engine configuration with the OGVs. Additionally, the acoustic dataset contains tonal mode measurements (Heidelberg, 2002), a spinning mode decomposition of the wall sound pressure levels (SPL) (Premo and Joppa, 2002), and far-field SPL measured along a sideline translating microphone probe. A brief description of the data processing performed and the location of the measuring probes is provided in Secs. II.A and II.B.

## A. Interstage Velocity Data

Single-point hot-wire probe measurements of the flow-field at station  $x=0.1016\,\mathrm{m}$  were collected to quantify the velocity field downstream of the fan wake. Figure 3 illustrates where the data collection takes place with respect to the fan stage. The dataset contains axial, tangential and radial velocity measurements acquired at a sampling rate of  $200\,\mathrm{kHz}$  for a duration of 1 second, totaling 129 fan revolutions. The data collected allows for the analysis of the frequency content in the velocity field in the interstage region. Power spectral densities (PSD) of the signals acquired for the axial, tangential and radial velocity components are computed with a bandwidth of  $28.6293\,\mathrm{Hz}$  using Hann windowing with a  $50\,\%$  window overlap to reduce spectral leakage.

#### **B. Far-Field Acoustics Data**

Acoustic data collection took place in the NASA SDT experiment along a sideline microphone array located 89.3 in (or 2.26822 m) away from the fan stage centerline. The geometric polar angles ranging from 25° to 130° are covered with varying resolution along the traversing sideline, while 3 additional microphones are fixed at the downstream station, covering the polar angles of 136°, 147° and 158°, for a total of 51 microphone locations. These locations are illustrated in Fig. 4. The experimental dataset includes sound pressure level (SPL) spectra at each microphone location.

## III. Computational Methodology

The CFD solver used in the present work is part of the Launch, Ascent, and Vehicle Aerodynamics (LAVA) solver framework (Kiris et al., 2016). This flexible computational framework was developed with highly complex geometries in mind. As such, it supports a variety of mesh paradigms, such as the structured Cartesian, curvilinear overset and unstructured arbitrary polyhedral grid types. In the present work, a conservative finite difference formulation is applied to the flow equations for non-orthogonal curvilinear coordinates in strong conservation law form (Vinokur, 1974) using an implicit second-order BDF2 time integration scheme. A Geometric Conservation Law (GCL) preserving time-varying metric term discretization is used for the moving grid system (Housman and Kiris, 2016). The computational domain is discretized using a set of structured curvilinear meshes, coupled together using an overset grid paradigm (Steger and Benek, 1987) and a sliding mesh interface methodology previously described in Fernandes et al. (2023). Finally, both Message Passing Interface (MPI) and OpenMP protocols are leveraged to achieve a highly scalable, parallel, HPC (High Performance Computing) code Kiris et al. (2016).

For the uRANS studies discussed in the present work, the Favre-averaged RANS system of equations is closed using the Spalart-Allmaras (SA-neg variant) turbulence model (Spalart and Allmaras, 1992). This modeling paradigm lacks the ability to capture the level of fine-grained turbulent content required to accurately predict broadband noise, and is thus

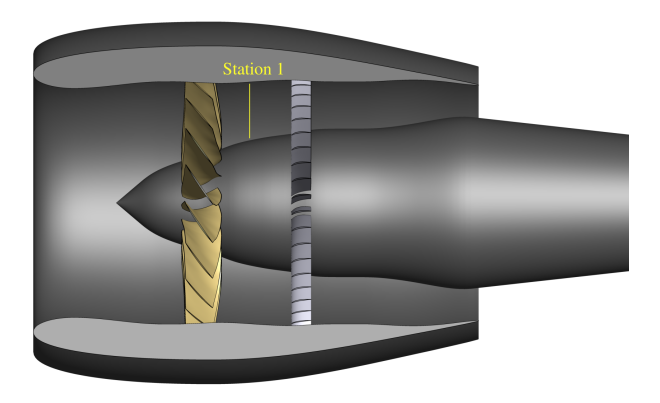


Fig. 3 Location of hot-wire probe station 1 in the interstage region.

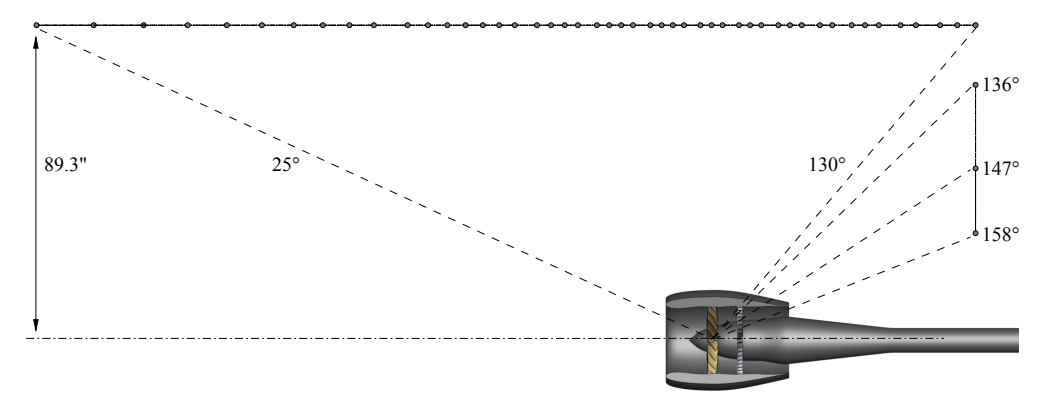


Fig. 4 Microphone locations in the experimental setup of the NASA SDT test.

only expected to capture tonal noise at BPF harmonics. On the other hand, hybrid RANS/LES employs a scale-resolving zonal DES model that provides LES behavior everywhere in the flow-field (LES mode) except for thin near-wall regions in attached boundary layers, where a RANS closure is applied (RANS mode). Regions treated in RANS mode can be defined explicitly, e.g. via an upper limit on the wall distance, or be detected by the model using a shielding function  $f_d$ , whose purpose is to protect the boundary layers from LES mode treatment - the reasoning being that RANS models accurately predict attached boundary layer development at a fraction of the mesh resolution requirements of LES. Both approaches are utilized in this work. Specifically, the model employing a shielding function to detect attached boundary layers used in the present work is the ZDES2020 Mode 2 Enhanced-Protection (EP) (ZDES-Mode2-EP) proposed by Deck and Renard (2020). The two main developments in the ZDES2020-Mode2-EP model over previous iterations of hybrid RANS/LES closures such as DDES2006 (Spalart et al., 2006) and ZDES2012-Mode2 (Deck, 2012) are an improved shielding function, offering better protection for zones that should stay in RANS mode, as well as a RANS-to-LES mode transition free of the delay in LES content creation typically observed in hybrid RANS/LES of free shear-layer flows. This methodology has been recently applied to the prediction of open rotor tonal noise using the LAVA solver framework (Dumlupinar et al., 2023) with success.

Different convective flux discretization approaches have been explored with the goal of identifying the extent to which numerical dissipation impacts broadband noise prediction in the far-field. One approach is a second-order convective flux discretization, consisting of a modified-Roe scheme with third-order left/right state reconstruction (Housman et al., 2009a,b) with the option of a Koren limiter (Koren, 1993). The second approach reduces the inherent artificial dissipation via a sensor that is applied to the left and right state reconstructions. As the sensor approaches zero the left and right state reconstructions approach an identical 4th-order centered reconstruction which eliminates the artificial dissipation and reduces the dispersion error of the convective flux discretization. In this work the sensor is evaluated as a combination of a vorticity and strain rate magnitude sensor that distinguishes between turbulent flow dominated regions and potential flow regions combined with a wiggle sensor that identifies odd/even decoupling in the pressure field. If the wiggle sensor is activated or the flow is identified as potential flow dominant then the dissipation is locally increased otherwise a more centered (less dissipative) discretization is utilized. Far-field acoustics are computed from integration of the FW-H equation written in the frequency-domain (Lockard, 2002) in a permeable surface formulation (di Francescantonio, 1997). The quadrupole term requiring volume integration outside of the enclosed FW-H surface is neglected in the present work.

## A. Geometry and Computational Domain

The baseline SDT configuration, shown in Fig. 2, is composed of four main components, namely the nacelle, centerbody, the R4 fan and the baseline OGV blade row. We refer to the internal surface of the nacelle as the casing. The origin of the coordinate system is located at the axial location corresponding to the rotor stacking axis along the centerline. The nacelle length is  $1.6\,D_{\rm f}$ , extending from  $x=-0.3305\,{\rm m}$  to  $x=0.5587\,{\rm m}$ . The 0.5 mm gap between the rotor blade tip and the casing is resolved in all simulations considered. The spinner part of the centerbody extends from the nose down an axial coordinate of  $x=0.0424\,{\rm m}$ . Downstream of this junction, the centerbody is stationary, and the wall boundary conditions applied in the computational setup properly reflect this behavior. Finally, the nacelle exit diameter is  $D_e=0.542\,{\rm m}$ .

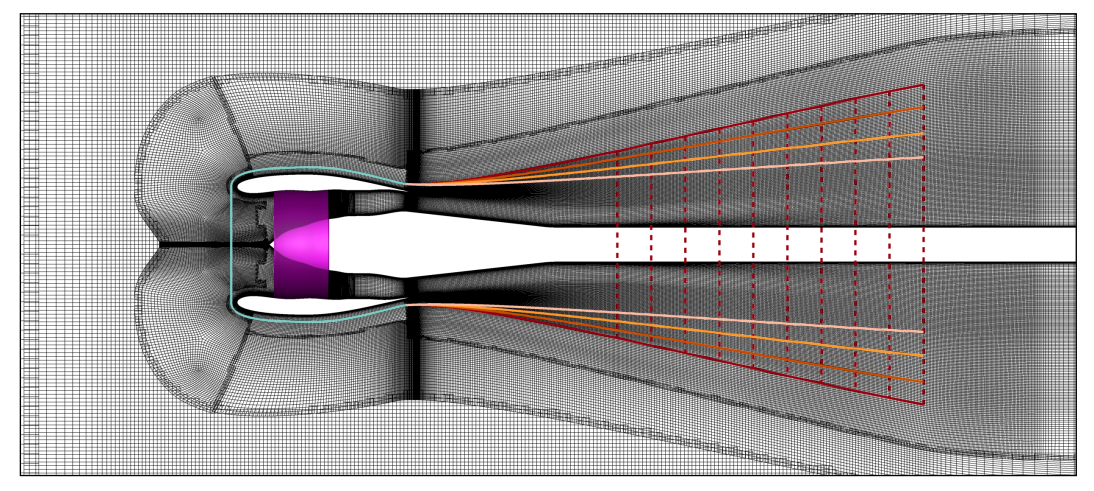
The wind tunnel mounting hardware was not modeled in the present work, so as to avoid the additional complexity and potential noise sources due to interactions of the shear-layer flow-field with these components. Correspondingly, the centerbody is extended axially downstream where grid stretching is applied to transition from the resolved near-field region to the under-resolved far-field. The incoming flow is aligned with the fan axis with a Mach number of 0.1. Farfield Riemann invariant boundary conditions are applied at the boundaries of the computational domain, with ambient static conditions of 101,325 Pa and 288.15 K. Adiabatic no-slip wall boundary conditions are applied at every wall in the domain, with the exception of the centerbody extension where a slip-wall boundary condition is applied and the boundary layer resolution is coarsened to lower the grid point counts.

#### **B. Grid Topology**

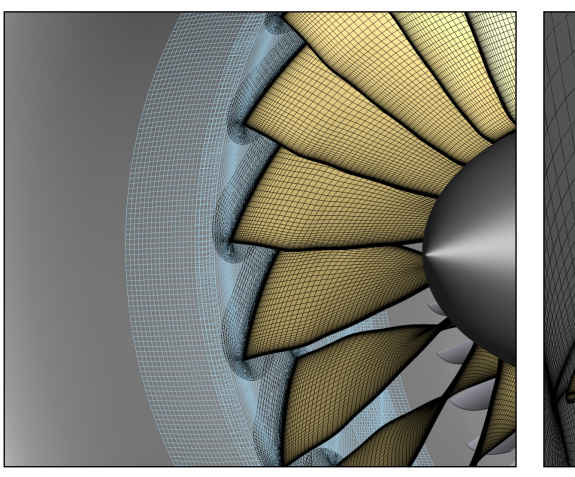
As mentioned above, the overset grid paradigm is used in the present work. An overview of the near-body grid topologies around the fan stage is shown in Fig. 5(a), which contains slices of relevant grid blocks with minimal overlap in overset regions on the Coarse level grid. It should be noted that the grid topologies have changed slightly from those presented in Fernandes et al. (2023) and Stich et al. (2022), although this is not expected to significantly change the conclusions derived from those studies. Finally, the grids were generated with hybrid RANS/LES best-practices

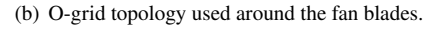
established from prior studies using the LAVA curvilinear solver (Browne et al., 2022; Kiris et al., 2022). This allows for a direct comparison of uRANS and hybrid RANS/LES on the same underlying computational grids.

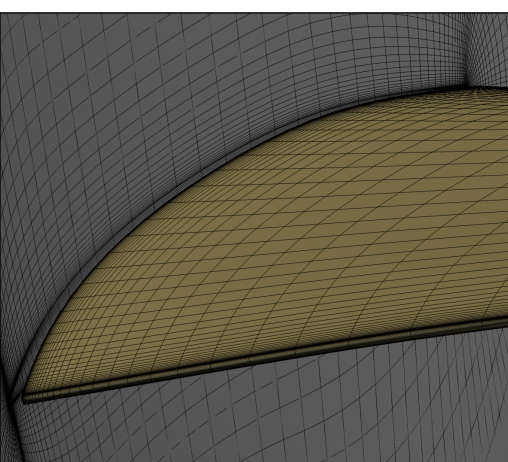
Most internal flow grids consist of block-structured point-matched grids, with the exception of the ones resolving the rotor and OGV blade geometries. These use overset to communicate with the nacelle inflow, interstage and outflow grid blocks. The grid sections shown are revolved 360° around the fan axis with varying circumferential grid point counts, with the exception of the off-body grid block covering the spinner nose tip to remove the geometric singularity that would otherwise occur. This block overlaps with the volume grid grown from a small surface cap grid covering the tip of the spinner nose. Cartesian grid blocks with a 2:1 coarsening ratio surround the near-field and create a smooth transition into the far-field. The region highlighted in purple represents the grid regions that rotate at the fan speed. These communicate with the upstream and downstream grids via a sliding mesh interface.



(a) Overview of near-body grid topologies. The profiles of the different FW-H permeable surfaces employed for the computation of the acoustic levels are also shown. Inlet surface region is shared across all surfaces (——), while the exhaust surfaces fan out away from the shear-layer. These surfaces include an inner-most (——), inner (——), outer (——) and outer-most (——) variants. The dashed lines (- - -) represent the location of outflow end-caps to perform averaging of the jet stream crossing the downstream end of the FW-H surface.







(c) Rotor tip region highlighting the  $0.5\,\mathrm{mm}$  gap.

Fig. 5 Overview of the grid topologies employed in the numerical simulations.

The surface grids near the fan blades can be visualized in Figs. 5(b) and 5(c). An O-grid topology is utilized to discretize the fan and OGV blades, with localized point clustering near the leading and trailing edges. In the spanwise direction, the grid stretches from wall-spacing near the hub, then reaches a constant spanwise spacing region around the mid-span, and finally refines down to wall-spacing again in the blade tip section.

Table 1 summarizes details for the grid family utilized in this work. Three grid levels - labeled Coarse, Medium and

Fine - were generated, with grid point counts ranging from 194 million to 1.182 billion. For each of these, estimates of the minimum number of points-per-wavelength (PPW) for the first two BPF harmonics at the low-speed regime are also provided in Table 1. These were estimated based on the maximum of the three computational index grid point spacings running along a streamline that goes through the fan stage and onto the exhaust. Figure 6 shows the variation of the estimated PPW along the stream-wise coordinate in the near-field. For the Medium grid level, the BPF<sub>1</sub> acoustic wave is resolved with between 20 and 40 points, while the BPF<sub>2</sub> one will have between 10 and 20.

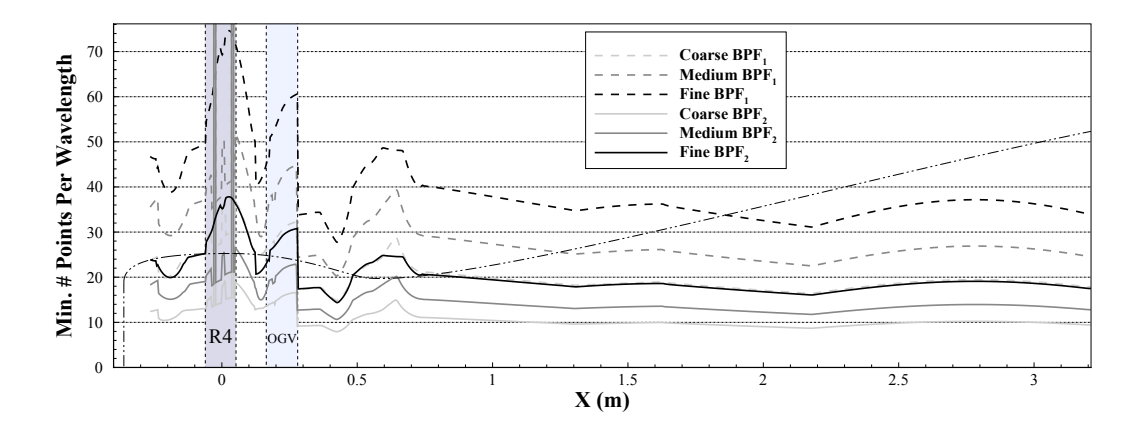


Fig. 6 Minimum points-per-wavelength (PPW) estimated along the engine for the low-speed regime. An outline of the profile of the FW-H surface (----) is also plotted as a function of the stream-wise coordinate.

Table 1	Summary of grid statistics	generated for the simulations i	performed in the present work.
I abic I	Dullilliai v OI El la statistics	Echici accu ioi the simulations	periorinea in the present work.

	Grid Level	# Grid Points [×10 <sup>6</sup> ]	Wall-Spacing [m]	Low-Speed Minimum PPW	
	Ec (c)	[//10 ]	[]	BPF <sub>1</sub>	BPF <sub>2</sub>
•	Coarse	194	$8.3 \times 10^{-6}$	15	8
	Medium	486	$7.0\times10^{-6}$	20	11
	Fine	1182	$5.0 \times 10^{-6}$	28	14

#### C. FW-H Surface Topology

This section provides details on the FW-H surfaces employed to store the near-field flow information prior to solving the FW-H equation to propagate the the acoustic signal onto the far-field. The solution information is interpolated onto the FW-H surfaces using a trilinear interpolation scheme at every time-step. To minimize the computational cost associated with file I/O, the writing of these interpolated solution files is buffered for a number of time-steps corresponding to half a fan revolution, and multiple time-steps are written at once in parallel.

To assess the sensitivity of the far-field acoustics to the topology of the FW-H surface, several different surfaces were generated. All of these surfaces share the fact that they are obtained by revolving a curve around the centerbody axis, i.e., they are circumferentially symmetric. Several of these curves are illustrated in Fig. 5(a). The profiles for these curves (labeled *inner-most*, *inner*, *outer* and *outer-most*) vary in the amount they fan out away from the shear-layer. The benefits of being able to utilize an FW-H surface closer to the shear-layer include not only an improved refinement level for the same number of points, but more importantly the potential to coarsen the underlying CFD grid at a lower radial coordinate and therefore lower the computational cost associated with the simulations. The first benefit is highlighted in Table 2, which summarizes details relative to each FW-H surface grid. The solution file sizes are provided for each surface grid, showing a savings of 61 GB per fan revolution in data that is written to disk between the *outer-most* and *inner-most* surface files. Also note that since the surface grids were sized based on a fixed edge spacing, the *outer-most* FW-H surface ends up with 30 % more grid points.

Furthermore, one must consider a level of refinement adequate for the FW-H surface in relation to the underlying CFD mesh. An incentive to utilize a coarser interpolation surface mesh exists, since it would amount to a lower computational cost for the FW-H propagation step, as well as a smaller disk footprint for the storage of the solution at each time-step, which for fan noise problems can be significant since several fan revolutions are often desired for the averaging window. Sensitivity to this interpolation surface grid spacing is assessed in section IV by considering far-field acoustic results obtained with three refinement levels of the *inner* surface illustrated in Fig. 5(a). As highlighted in Table 2, the file storage requirements for a single fan revolution between Coarse, Medium and Fine FW-H surface grid levels ranges from 30 GB to around 450 GB.

The question of whether or not to close the outflow boundary where the shear-layer turbulence crosses the FW-H surface (violating the assumption that all noise sources are contained within said surface) is also assessed by comparing far-field spectra with an open end, a single closing end-cap, and several closing end-caps placed equidistantly over which the solution is averaged. These end-caps are illustrated in Fig. 5(a) with dashed lines for the *outer-most* FW-H surface. Finally, the effect of neglecting part of the FW-H surface that goes over the nacelle - where acoustic sources are expected to be negligible - is also investigated by comparing solutions taken with the *inner* FW-H surface and an equivalent surface with disjoint inlet and exhaust regions. This surface - labeled *inner-separate* - will also help determine the inlet and exhaust contributions to the overall far-field noise. Results for the different FW-H surfaces described here are discussed in Sec. IV.

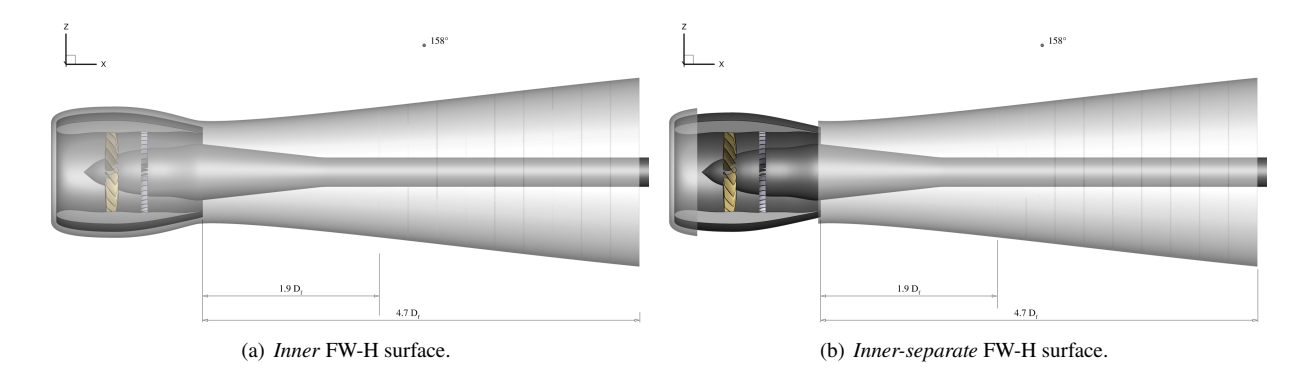


Fig. 7 Overview of the *inner* and *inner-separate* FW-H surfaces generated.

Table 2 Summary of the FW-H surfaces studied. All surfaces use a baseline edge spacing of 5 mm, except for the Fine and Coarse refinement versions of the *inner* surface, which utilize a baseline edge spacing of 2.5 and 10 mm, respectively. Outflow treatment symbol legend: |||| outflow end-cap averaging,  $\odot$  open end outflow,  $\otimes$  closed end outflow end-cap.

Label	Outflow Treatment	Number of Cells	Edge Spacing [mm]	Edge Ratio to CFD Mesh	Grid File Size [MB]	Solution File Size [GB/Rev]
Inner-most		864,724	5	1:1	26	97
Inner (Coarse)		213,150	10	1:2	7.5	30
Inner (Medium)		931,138	5	1:1	30	114
Inner (Fine)		3,699,190	2.5	2:1	117	449
Inner-separate		812,428	5	1:1	27	105
Outer		1,022,392	5	1:1	36	137
Outer-most	$\odot \otimes    $	1,116,386	5	1:1	42	158

#### IV. Results and Discussion

In this section, the results of the uRANS and hybrid RANS/LES simulations performed in the context of the NASA Source Diagnostic Test case are discussed. The presentation of these results is divided into two subsections, one devoted to the analysis of the near-field flow and a second one dedicated to a description of the far-field acoustic predictions. The near-field flow analysis includes a breakdown of the interstage velocity field power spectral densities (PSD) as well as flow visualizations of the sound-wave patterns around the rig as described via the time derivative of the pressure field. Far-field acoustic predictions include sound pressure levels (SPL) along the sideline illustrated in Fig. 4, overall sound pressure levels (OASPL) around the hemisphere, as well as sound power levels (PWL) estimated from integration over the hemisphere. Several sensitivity studies were performed including grid sensitivity effects as well as studies on several parameters relating to the FW-H acoustic propagation step. This section ends with a study on the effect of blade stagger angle irregularities around the wheel, an original contribution of the present publication that builds upon a similar study performed at the high-speed regime in Gonzalez-Martino and Casalino (2018).

Coarse grid level simulations were initialized from precursor unsteady RANS simulations using a large time-step and about thirty rotor revolutions to convect the initial transient out of the resolved near-field domain. The time-step was then dropped to the production run value, and simulations were carried out for a minimum of 15 rotor revolutions to produce mature solutions from which to extract turbulent flow statistics and data for acoustic post-processing. Both uRANS and hybrid RANS/LES coarse grid solutions were initialized using this procedure. The subsequent grid levels (Medium and Fine) were initialized by interpolating the mature solution from the preceding grid level and letting the flow mature for another 15 rotor revolutions on the refined grid.

Table 3 presents a summary of the production simulations performed. All uRANS simulations utilize the third-order upwind scheme (labeled upwind) described in Sec. III. The hybrid RANS/LES results, on the other hand, explore the differences observed between this third-order upwind scheme and the low-dissipation blending scheme (upwind-blend), where the upwind blending factor  $\psi_{upwind}$  was kept to a low value of 0.02. Another important distinction between the upwind and upwind-blend simulations is the explicit definition of the regions in the flow treated in RANS mode in the latter. This is accomplished by specifying a distance away from the walls outside of which a Smagorinsky-like turbulent length scale is utilized in the transport equation for the eddy viscosity. This distance was determined from average boundary layer thickness measurements in the interstage region for the upwind simulations, and was set to 4 mm in the upwind-blend simulations. Therefore, hybrid RANS/LES simulations that combine the upwind convective flux scheme and the enhanced-protection shielding function are labeled ZDES-Mode2-EP Upwind, while those using the upwind-blend scheme and a simple wall-distance inspection for RANS mode treatment are labeled ZDES Upwind-U

The simpler ZDES model was employed in the ZDES Upwind-Blend simulations as a way to circumvent the delay in transitioning from RANS to LES mode downstream of the fan blades, which was observed in the ZDES-Mode2-EP Upwind simulations employing the  $f_d$  function proposed by Deck and Renard (2020). This behavior is visualized in Fig. 8, which compares contours of the shielding function  $f_d$  between the ZDES-Mode2-EP Upwind and ZDES Upwind-Blend simulations. In the ZDES-Mode2-EP Upwind case, the shielding of the boundary layers forming around each blade extends far downstream (until around the axial location of the hot-wire station 1 shown in Fig. 3), delaying the generation of small scale turbulence in the blade wakes. This, in turn, sustained the large-scale coherence of the fan blade wakes instead of promoting their breakdown, causing an over-prediction of the rotor-stator interaction tonal noise. This observation is further discussed in Sec. IV.

The time-step was selected using a points-per-period (PPP) metric based on BPF<sub>2</sub>. For the simulations employing the *upwind* convective flux scheme, a time-step corresponding to 25 PPP for both uRANS and hybrid RANS/LES cases. All *ZDES Upwind-Blend* simulations double the BPF<sub>2</sub> resolution relative to the corresponding *ZDES-Mode2-EP Upwind* cases in an attempt to extend the frequency range of the far-field acoustic predictions. This finer time-step of 50 PPP was also tested on the Coarse mesh using the *ZDES-Mode2-EP Upwind* simulations, to understand if the improvements in the far-field noise predictions obtained were time-step related. However, apart from raising the high-frequency broadband noise levels as expected, the smaller time-step simulation still showed the same spurious tonal noise sources identified in the 25 PPP case.

#### A. Near-Field Flow Analysis

The discussion begins with an analysis of the spectral content of the interstage velocity field. A time history of 10 fan revolutions was used when computing the PSD for each of the three velocity components (axial, tangential and radial) using Welch's method with a bandwidth of  $28.6293 \, \text{Hz}$  and  $50 \, \%$  overlap. Figure 9 shows carpet plots of the hot-wire data PSD and the three low-speed numerical results obtained on the Medium grid level, where the vertical

Table 3 Summary of production simulations conducted for the low-speed regime.

Turbulence Model	Modeling Approach	Time-steps per Rev	PPP <sup>a</sup> for BPF2	Grid Level	CPU Time <sup>b</sup> (node hours / Rev)	Turn-around Time (days / 10 <sup>3</sup> cores)
uRANS (SA-neg)	Upwind	1078	25	Coarse Medium Fine	-	-
	ZDES-Mode2-EP Upwind -	1078	25	Coarse	-	-
		2156	50	Coarse		
Hybrid		1078	25	Medium	-	-
RANS/LES	ZDES Upwind-Blend	2156	50	Coarse	346	8.4
				Medium	1068	26.7
				Fine	2773	69.3

<sup>&</sup>lt;sup>a</sup> Points-per-period.

<sup>&</sup>lt;sup>b</sup> Estimated using Electra SkyLake nodes with 40 cores per node while fixing the number of grid points per core at different grid levels.

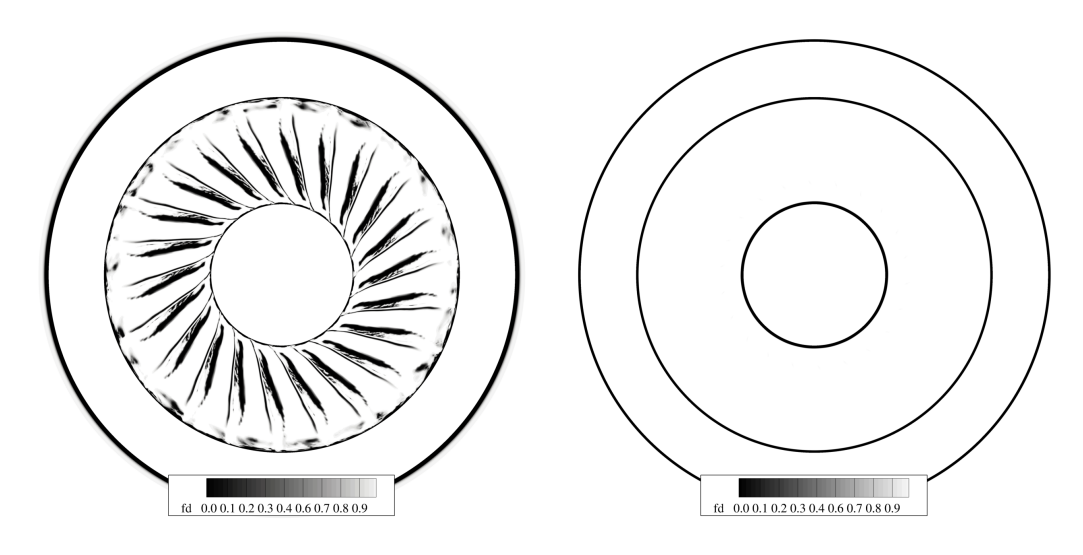


Fig. 8 Shielding function  $(f_d)$  contours for the ZDES-Mode2-EP Upwind (left) and ZDES Upwind-Blend (right) simulations at X = 0.05 m. Black regions  $(f_d \rightarrow 0)$  correspond to regions of the flow treated in RANS mode, while in white regions  $(f_d \rightarrow 1)$  the flow is treated in LES mode.

coordinate corresponds to the radial coordinate along the hot-wire probe normalized between 0 (hub) and 1 (casing).

Streaks corresponding to each BPF harmonic are clearly observed in the experimental PSD (top row). A significant amount of broadband content is also visible near the casing (downstream of the blade tip region), with amplitudes decaying with frequency. Mid-span broadband content is concentrated between 25 % and 80 % span and remains high until around BPF<sub>6</sub>. Unsteady RANS (second row) correctly predicts the location of the BPF harmonics in the velocity field, but no broadband content is visible in the PSD plot due to a lack of small scale turbulent content. In contrast, both hybrid RANS/LES simulations show evidence of broadband content present, together with the correct prediction of the high amplitude streaks corresponding to BPF harmonics. The ZDES Upwind-Blend simulation (bottom row), however, is observed to introduce streaks at certain non-BPF harmonics that are not observed in the experimental PSD or the ZDES-Mode2-EP Upwind run (third row). These qualitative comparisons also show that the mid-span and tip region velocity field broadband content is visibly under-predicted in all simulations.

A quantitative comparison is presented in Fig. 10. Several observations stand out from these plots. The *ZDES Upwind-Blend* result shows higher-amplitude high-frequency content near the hub, indicative of the presence of small

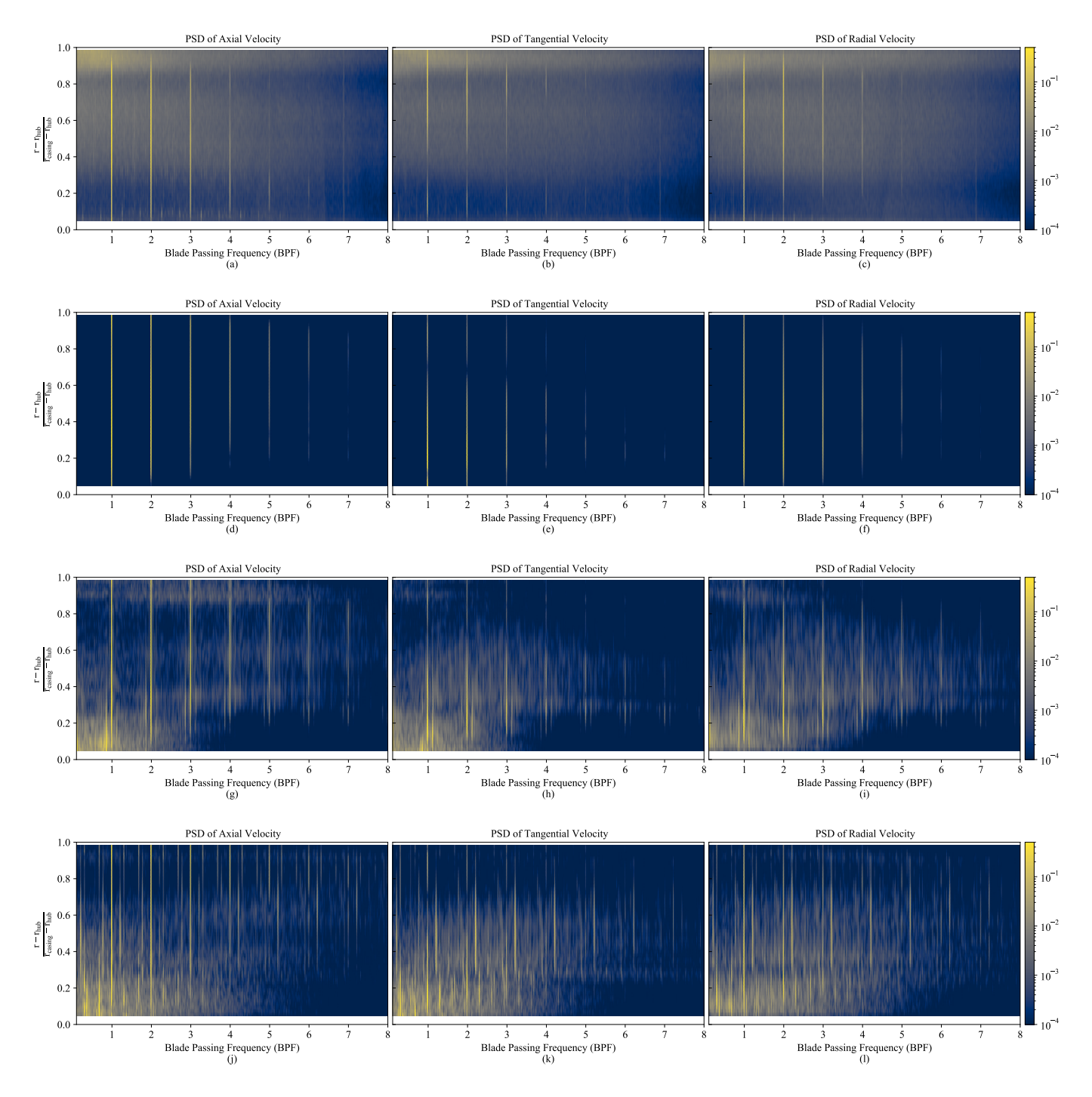
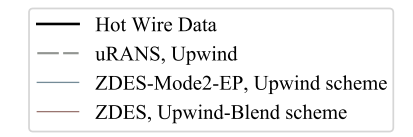


Fig. 9 Power spectral density (PSD) carpet plots of interstage velocity field. From left to right, the PSD of axial, tangential and radial velocity components are shown, respectively. From top to bottom, the hot-wire experimental data (first row), uRANS (second row), ZDES-Mode2-EP, Upwind (third row) and ZDES, Upwind-Blend (final row).

scale turbulent structures; this scheme is also able to redistribute into other frequencies some of the BPF-locked energy in the *ZDES-Mode2-EP Upwind* simulation due to the excessive coherence of the blade wake structures - note the drop in BPF<sub>1</sub> tone level in Fig. 10(b) and BPF<sub>3</sub>, BPF<sub>4</sub> and BPF<sub>5</sub> tone levels in Fig. 10(d). However, the less dissipative scheme comes with its own set of inaccuracies - starting with a spurious tone at normalized frequencies of 0.22 + nBPF, and showing lower broadband content in the blade tip vortex region. The latter can be explained by the thicker shielding

of the boundary layer in the *ZDES Upwind-Blend* case in Fig. 8(b), where the flow is kept in RANS mode over a larger distance away from the casing wall when compared to the *ZDES-Mode2-EP Upwind* run shown in Fig. 8(a). Given the small tip gap spacing of just 0.5 mm, it is likely that a large portion of the blade tip vortex region is within this RANS-shielded portion of the domain, where all smaller scales that would lead to a broadband spectra are dissipated. This possibility will be investigated in the future.



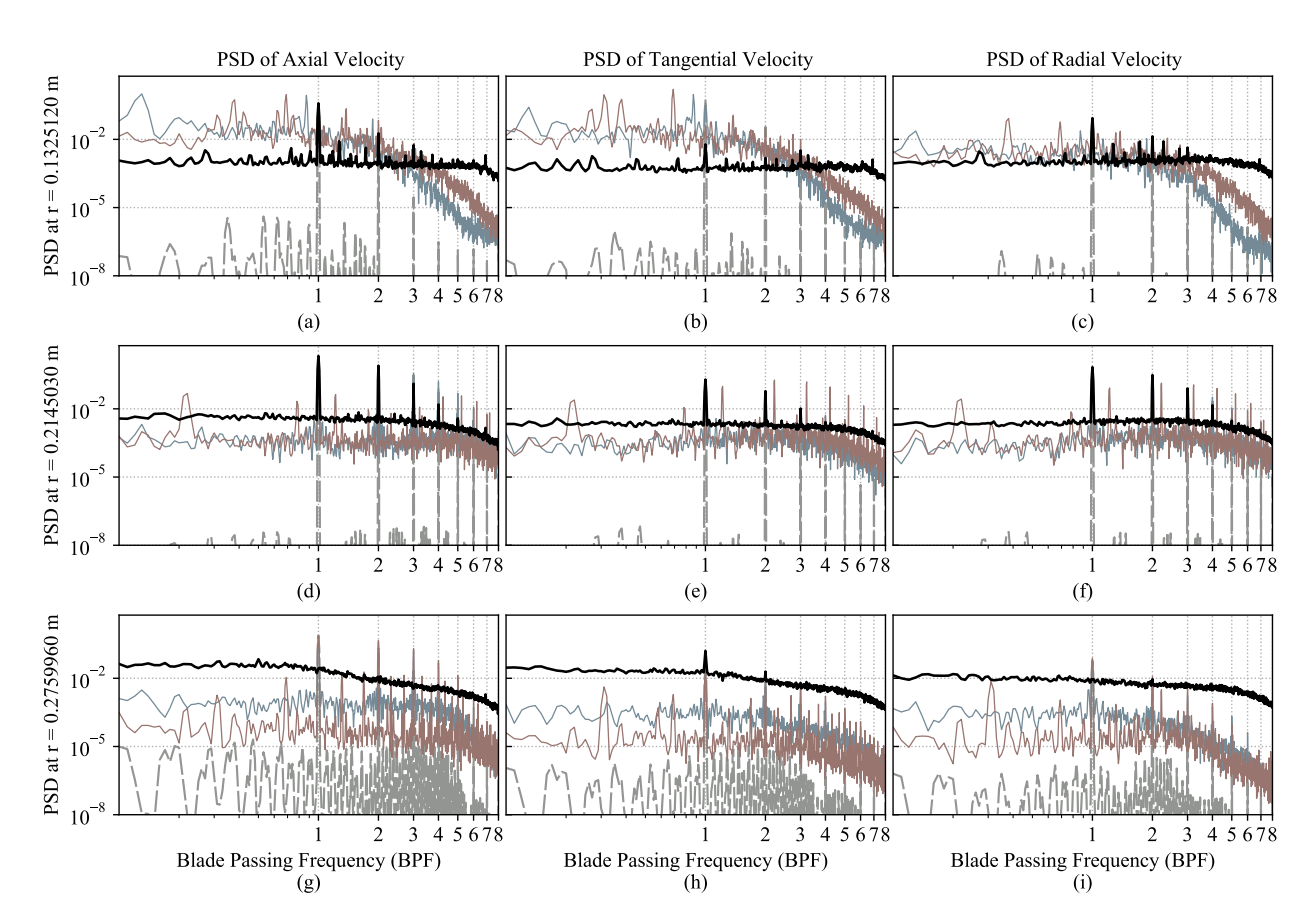
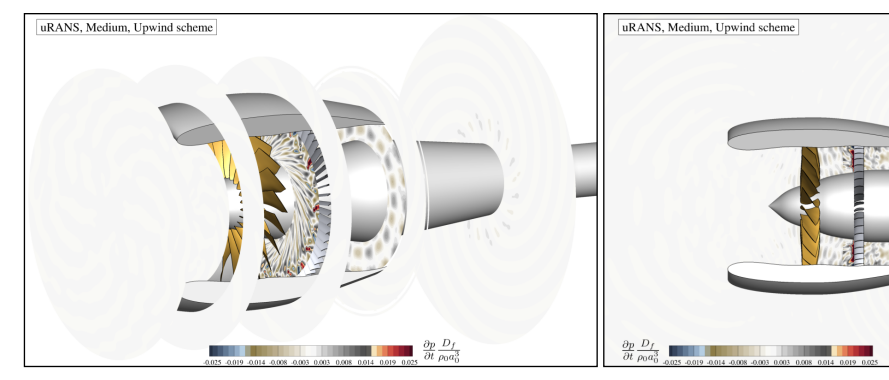
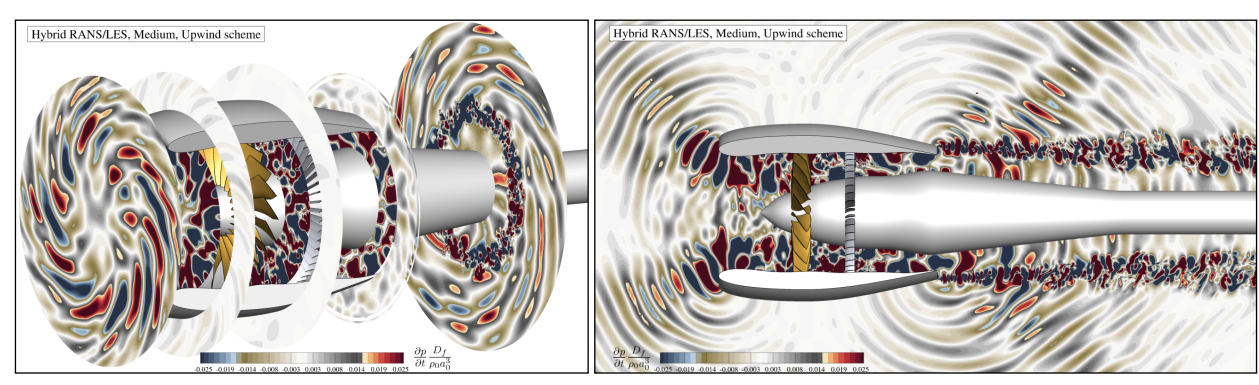


Fig. 10 Power spectral density plots of the velocity field at three radial stations. Top row (r = 0.1325120 m) is near the hub, middle row (r = 0.2145030 m) is in the mid-span region and bottom row (r = 0.2759960 m) is near the casing, downstream of the blade tip.

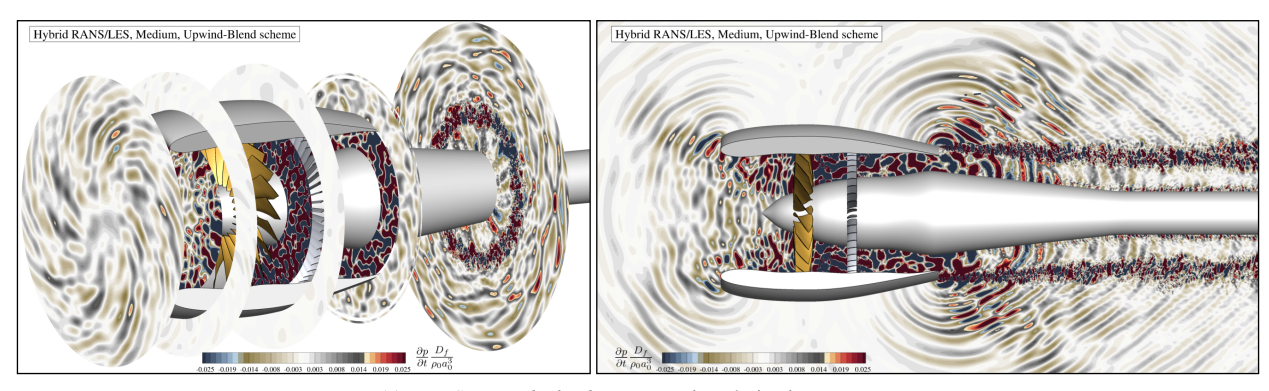
Figure 11 illustrates the sound wave patterns emanating from the turbofan model for the three modeling strategies employed on the Medium grid level. Unsteady RANS (Fig. 11(a)) clearly misses essentially all fore-propagating noise, and significantly under-predicts the aft-propagating sound waves when compared to both hybrid RANS/LES approaches. For the present rotor-stator configuration, the BPF<sub>1</sub> tone is cut-off at the low-speed regime, which explains why no sound waves propagate upstream in the uRANS simulation - virtually all fore-propagating noise is broadband in nature. Despite this, the *ZDES-Mode2-EP Upwind* hybrid RANS/LES simulation (Fig. 11(b)) shows a strong fore-propagating tone that is more intense than the background broadband noise. Based on the discussion above, this tone should not be present. The delay in the breakdown of the blade wakes in the interstage region, which was observed for this simulation, is thought to be responsible for the presence of this spurious tone, via the impingement of those large-scale coherent wake vortices on the OGVs. When the lower-dissipation *upwind-blend* scheme is combined with the explicit assigning of flow regions treated in RANS mode to those within 4 mm away from walls, the fore-propagating tone present in



(a) Unsteady RANS - pressure time derivative contours.



(b) ZDES-Mode2-EP Upwind - pressure time derivative contours.



(c) ZDES Upwind-Blend - pressure time derivative contours.

Fig. 11 Sound-wave patterns visualized via normalized pressure time derivative contours.

the ZDES-Mode2-EP Upwind run is no longer present. Figure 11(c) also shows the presence of smaller-scale waves which the low-dissipation scheme is able to retain, and improved broadband wave patterns in the aft-propagating portion of the domain. Finally, the spiral wave patterns observed in the axial slices for both hybrid RANS/LES simulations appear significantly more disrupted in the ZDES Upwind-Blend simulation, due to the larger amount of turbulent scales resolved in the low-dissipation scheme.

#### **B. Far-Field Acoustic Predictions**

In this section, the far-field acoustics results are analyzed and compared with the microphone data gathered in the experiment. The permeable surface FW-H approach is utilized to propagate the near-field acoustics onto the far-field microphone locations using a frequency-domain formulation of the FW-H equation. Four sets of data are analyzed throughout this section:

- Narrow-band power spectral density (PSD) spectra at the observer locations corresponding to the sideline microphone array shown in Fig. 4;
- Overall sound pressure levels (OASPL) along the same sideline microphone array, corresponding to integrating
  each observer spectra over the frequency domain, restricted to the range 1.2 kHz to 50 kHz in order to avoid
  contributions coming from the mounting rig in the measured spectra (Brown and Schifer, 2008);
- Narrow-band sound power level (PWL) calculated by integrating the acoustic intensity over the hemisphere covered by the sideline microphone array, using the same formula presented in Gonzalez-Martino and Casalino (2018), repeated here for convenience:

$$PWL(f) = \int_{\theta_{\min}}^{\theta_{\max}} 2\pi R^2 \sin(\theta) \frac{\left[1 + M_{\infty} \cos(\theta)\right]^2 PSD(f, \theta)}{2\rho_{\infty} c_{\infty}} d\theta, \tag{1}$$

where  $M_{\infty}$ ,  $\rho_{\infty}$  and  $c_{\infty}$  are the freestream Mach, density and sound speed, R is the distance away from the source, taken here as the coordinate system origin,  $\theta$  is the radiation angle between the centerline and each observer angle along the sideline array, and  $PSD(f,\theta)$  is the power spectral density at each observer location. Note that the formula is typically utilized to perform the integration using observer locations at a fixed radius along a circular hemispherical array. Since no such array was utilized in the experiment, the PSD values measured along the sideline microphone array are used in Eq. 1. Using this approach, one must consider the radial distance variation between observers, which is taken into account by varying the radial coordinate R in the integrand. Tests performed using simulation data comparing this approach with a traditional circular array located at a fixed radius of 10 m have shown negligible differences between the two (Fig. 12(f));

 Sound pressure levels (SPL) at discrete BPF harmonics are also extracted from the spectra and compared across different observers to compare tone levels directly.

The near-field flow is sampled at every time-step for a sampling window no shorter than 5 rotor revolutions. The time-histories of the sampled flow quantities are Fourier-transformed using Hann windowing with 50 % overlap, and the spectra is normalized to conserve total energy. The window length  $(n\Delta t)$  is chosen such that two constraints are satisfied:

- 1) An integer number (a) of blade-passing-periods (BPP) per window are utilized to prevent aliasing, corresponding to  $aN/22 = aN^{bp}$  time-steps, where N is the number of time-steps per rotor revolution,  $N^{bp}$  is the number of time-steps per blade pass, and a is the number of BPP;
- 2) The resulting frequency spectra has a bandwidth  $\Delta f$  of 58.5 Hz, as given in the test data. In practice, this corresponds to finding the nearest integer satisfying

$$a = \frac{1}{\Delta t N^{bp} \Delta f}$$
, with  $\Delta f = 58.5 \,\text{Hz}$ , (2)

which guarantees that the resulting spectra has a bandwidth as close to the test data as possible while preventing aliasing by using an integer number of BPP. The total number of time-history samples covered by this procedure is then computed as

$$n_t = aN^{bp} [p(N^w - 1) + 1],$$
 (3)

where  $N^w$  is the number of Hann windows utilized and p=0.5, corresponding to  $50\,\%$  overlap between windows. For instance, the low-speed hybrid RANS/LES case simulated with 2156 time-steps per rotor revolution will have  $N^{bp}=2156/22=98$  time-steps per blade pass and a=48 blade-passing-periods per window. For a total sampling period covering at least 5 rotor revolutions ( $n_t>=5\times2156$ ), one would need  $N^w=4$  windows, each covering a=48 BPP (or  $\approx48/22=2.18$  rotor revolutions per window), for a total of  $n_t=11760$  time samples covering approximately 5.45 rotor revolutions (or 120 BPP). Sensitivity to the total number of BPP is presented in the following subsections, but typically this value is set such that only the last 120 BPP are taken into account.

Finally, far-field spectra are obtained after performing azimuthal averaging of the signals obtained at several equally-spaced observer locations around the turbofan. Sensitivity of the spectra to the number of azimuthal observers is also reported in the following discussion, but otherwise this number is set to 32, i.e. at every 11.25°.

**FW-H Sensitivity Studies** Sensitivity studies performed on several aspects of the FW-H approach will now be presented. Results for these studies rely on the time-histories obtained using the *ZDES Upwind-Blend* hybrid RANS/LES simulations ran on the Medium grid level. Figure 12 presents the results of several sensitivity studies for the low-speed operating condition. The FW-H surface employed for these results is typically the *outer-most* one, with the exception of the FW-H surface resolution sensitivity study, which uses the *inner* FW-H surface. With the exception of the FW-H

end-cap treatment sensitivity study shown in Fig. 12(c), all results were obtained using outflow end-cap averaging along the 10 end-caps illustrated in Fig. 5(a) following the approach recommended by Shur et al. (2005) and outlined in Mendez et al. (2013).

The sound power levels (PWLs) corresponding to sampling periods of 72, 120 and 168 BPP (corresponding, respectively, to approximately 3.27, 5.45 and 7.64 rotor revolutions) are shown in Fig. 12(a). According to the procedure outlined above, these were computed using two, four and six Hann windows, respectively. The three spectra show essentially the same character, apart from some small differences at the lower frequencies, which are especially noticeable between 72 BPP and 120 BPP. For this reason, the remaining spectra were calculated using a minimum sampling window of 120 BPP. Figure 12(b) shows the PWL spectra variation observed by using an increasing number of azimuthal averaging observers, starting at just 2 (every 180°) and going up to 32 (every 11.25°). Clear differences in the spectra are observed up to 16 equally-spaced observers. Local low-amplitude tones in the signals picked up with just 2 observers get averaged-out of the final spectra with an increasing number of azimuthal observers, and the frequency spectrum becomes smoother. Between 16 and 32 azimuthal observers, the differences are almost negligible. Up to 128 observers were utilized in our studies (not shown), with no discerning differences with the results obtained with 32 observers. In the remaining discussion, spectra were averaged from the signals obtained using 32 equally-spaced observers.

The effect of varying the FW-H end-cap treatment is analyzed in Fig. 12(c). Results are presented for the *outer-most* FW-H surface, with no outflow end-cap considered (open end), with a single outflow end-cap at the furthest downstream location shown in Fig. 5(a) (closed end), and using end-cap with an increasing number of outflow end-caps in an attempt to promote destructive interference in the hydrodynamic fluctuations crossing the downstream end of the FW-H surface. For the open end case, a shorter version (open end short) of the surface is also considered where the FW-H surface only extends downstream of the nacelle exhaust by 1.9 fan diameters (see Fig. 7). Results using the single closing end-cap show an over-prediction of the low-frequency content, caused by the crossing of large-scale low-frequency hydrodynamic fluctuations through this boundary. Performing end-cap averaging appears to be effective at lowering these spurious contributions. Differences between the open FW-H surface spectra and the end-cap-averaged one are strongest at low-frequencies, indicating that low-frequency hydrodynamic waves are present even after end-cap averaging. Since these differences are away from the mid- and high-frequency regions corresponding to BPF<sub>1</sub> and BPF<sub>2</sub>, end-cap-averaging is performed for the remainder of the results shown.

Next, different FW-H surface resolutions are compared using the inner FW-H surface variant. Results for the coarse, medium and fine FW-H surface resolutions, characterized by an edge ratio relative to the underlying CFD mesh of 1:2, 1:1 and 2:1, respectively, are plotted in Fig. 12(d). It is seen than coarsening the FW-H surface relative to the CFD mesh spacing can result in PWL differences of up to 1 dB. As expected, the trilinear scheme used to interpolate the flow solution to the FW-H surface does not lead to any benefits when refining the FW-H surface past the underlying CFD mesh spacing used. Figure 12(e) compares the PWL spectra obtained with the different FW-H surfaces described in Sec. III.C. Apart from the very high-frequencies which the numerical scheme used can't resolve anyway, no differences are visible in the spectra produced by the distinct surfaces. This suggests that significant savings in disk storage requirements could be achieved by fanning out the FW-H surface in the exhaust region as little as possible, while keeping the shear-layer hydrodynamic fluctuations within its bounds. The disk storage savings potential for the FW-H surfaces considered in the present work is on the order of 60 GB per rotor revolution, assuming the flow-field is sampled at every time-step. Figure 12(e) also shows that the PWL spectra of the inner and inner-separate are indistinguishable, indicating that all relevant noise sources are well captured by separation of the inlet and exhaust contributions as shown in Fig. 7(b). This will allow comparison of the total and inlet-only spectra available from the test in the subsequent discussion. Finally, Fig. 12(f) shows the agreement between using a circular microphone array at a fixed distance Rfrom the source and a sideline array with varying R in Eq. 1, thus validating the use of the sideline array for PWL calculations as outlined earlier.

**Turbulence Modeling Strategies** A comparison of the results obtained for the three simulations performed on the Medium grid level, namely, unsteady RANS and both hybrid RANS/LES variants will now be presented. Figure 13(a) shows the PSD for the three simulations at four different observer locations along the sideline microphone array, specifically 25°, 65°, 111° and 130°. The unsteady RANS results are shown (only visible at 111° and 130°) for completeness, but a discussion of these is deferred to the next section. The spectra obtained in the *ZDES-Mode2-EP Upwind* run shows a large spurious tone present at around 1.15BPF, which was identified to originate from the exhaust by breaking down the inlet and exhaust contributions using the *inner-separate* FW-H surface. Further analysis of pressure contours band-limited around the spurious tone revealed a strong interaction with the OGVs that was propagating

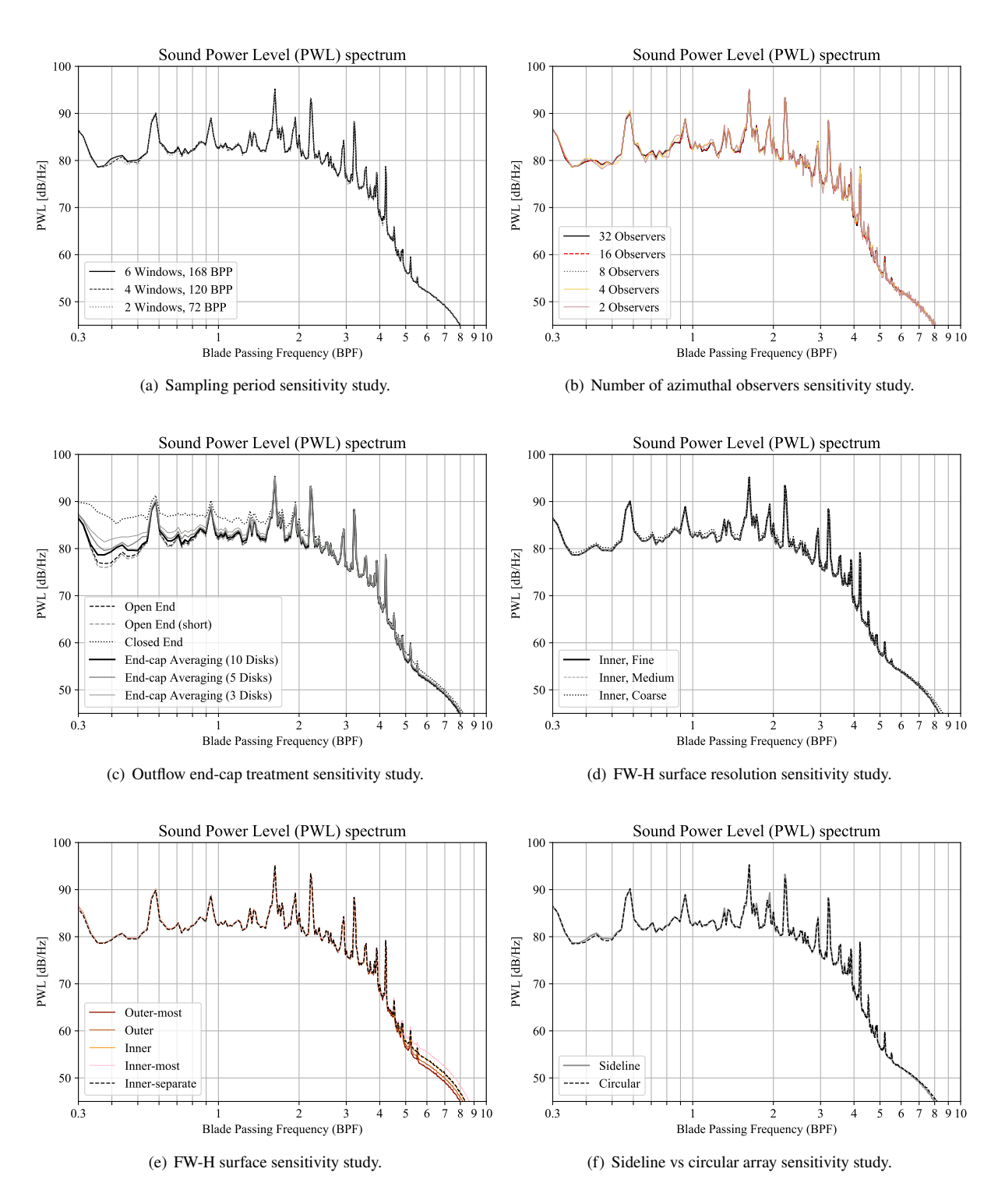


Fig. 12 Sound power levels (PWL) for several sensitivity studies performed in the context of different aspects of the FW-H approach using the results from the low-speed regime ZDES Upwind-Blend hybrid RANS/LES simulation on the Medium grid level.

onto the aft arc. This indicates the presence of nonphysically large coherent structures interacting with the stator row, which are suspected to result from the delayed transition to LES mode described at the start of this section. The *ZDES* 

Upwind-Blend run, armed with a lower dissipation convective flux scheme and able to circumvent this issue, appears to eliminate this spurious tone, while admittedly still showing other tones that are not present in the experimental data at 111° and 130°. The presence of the spurious tone in the ZDES-Mode2-EP Upwind run could not be attributed to the larger time-step size used in that simulation, as a run with the same time-step as the ZDES Upwind-Blend variant was attempted but still showed a strong tone at the same frequency. This time-step difference is, however, responsible for the improvement in the broadband noise levels observed at high-frequencies for the ZDES Upwind-Blend run. The spectra obtained with this variant shows overall good agreement with the experimental broadband noise levels up to BPF<sub>2</sub>.

The PWL spectrum shown in Fig. 13(b) follows the same considerations just described, with good broadband level agreement up to BPF<sub>2</sub> and some local spurious tones present which cause discrepancies of up to around 10 dB. As shown in the next section, the acoustic energy locked in these tones appears to get redistributed as the grid is refined past the Medium grid level. The OASPL along the sideline is shown in Fig. 13(c). Opposing trends are observed for the ZDES-Mode2-EP Upwind and ZDES Upwind-Blend runs in the inlet region - the latter under-predicts OASPL levels while the former over-predicts these up to around 90°, where the agreement between the two (and the experiment) is best. The two simulations closely follow the experimental data trend up to 110°, after which both over-predict OASPL levels, especially past 130°. Analysis of the PSD spectra for the three observer locations located past 130° reveals an over-estimation of the low-frequency broadband content. Finally Fig. 14 shows the BPF<sub>1</sub> (left) and BPF<sub>2</sub> (right) tones extracted at several observer locations, and compared with the experimental data (grey bar in the background). The ZDES Upwind-Blend simulations consistently shows predicted sound pressure levels closer to the experiment.

Grid Refinement Study Three grid levels were used to simulate both the uRANS and hybrid RANS/LES (ZDES Upwind-Blend variant) and assess grid convergence. For the ZDES-Mode2-EP Upwind case, only Coarse and Medium grid level results were explored. Figure 15 compares the BPF<sub>1</sub> and BPF<sub>2</sub> sound pressure levels across different observer locations along the sideline microphone array for the different grid refinements simulated. Focusing initially on Fig. 15(a), which shows the grid refinement results for the uRANS simulations, it is clear that BPF<sub>1</sub> SPL values are significantly under-predicted, even at the finest grid level. This indicates that broadband noise dominates the total noise signature around this frequency, which is in agreement with the earlier discussion about BPF<sub>1</sub> being an evanescent (cut-off) tone for the baseline SDT configuration at the low-speed regime. These broadband noise levels show some sensitivity with grid refinement, but the underlying RANS model dissipates any small-scale fluctuations that would lead to broadband noise before they have a chance to reach the FW-H surface. The equivalent plot for BPF2 shown on the right side now shows a significant increase in SPL due to the presence of a BPF2 tone that uRANS is able to capture. The trend of increasing SPL with observer location angle is associated with the dominance of the tonal component in the exhaust region, as evidenced by the tonal sound-wave patterns shown in Fig. 11. The results also show an over-prediction of the BPF<sub>2</sub> tone at the downstream observer locations past 130°. The large differences in the SPL levels observed between the Medium and Fine grid levels at BPF<sub>2</sub> suggests that a number of points-per-wavelength larger than 14 might be necessary for the *upwind* scheme for grid-converged solutions using uRANS.

Results for both hybrid RANS/LES simulations are shown in Fig. 15(b). The first thing to note, and one of the reasons why a Fine grid level simulation was not pursued for the ZDES-Mode2-EP Upwind case, is that the Medium grid refinement level results in worse SPL levels when compared to the Coarse grid level (especially at low-frequencies). Grid convergence of the BPF<sub>1</sub> tone in the ZDES Upwind-Blend approach appears to be primarily monotonic, and differences between the Fine and Medium grid levels are visibly lower than those between the Medium and Coarse grid levels, indicating a grid convergence trend. For BPF2 the trend is not monotonic with grid refinement, but values trend towards the experimental data, especially in the mid-sideline locations between 65° and 95°. Figure 16(a) shows the PSD at 4 observer locations spanning the sideline microphone array. Significant differences in the broadband levels are evident between the Coarse and Fine grid levels on the ZDES Upwind-Blend result. These broadband frequencies decay quickly past BPF<sub>1</sub> at the 25° observer location, potentially indicating a lack of grid resolution in the inlet section. A few nonphysical tones are observed across the spectra for the observer locations showed, with the most prominent one occurring close to BPF<sub>2</sub>. Nonetheless, the broadband noise levels at 65°, 111° and 130° show good agreement with the experimental values up to BPF<sub>2</sub>. Figure 16(b) compares the PWL spectra against the experimental data, showing the trends just discussed. Again, the broadband noise levels show good agreement with the experimental sound power levels up to about 2.5BPF. Noise directivity is analyzed in Fig. 16(c), which shows the overall sound pressure levels across the hemisphere. Here, the decrease in solution quality between the Coarse and Medium grid levels around the inlet for the ZDES-Mode2-EP Upwind simulations is evident. In addition, the inlet region shows that the OASPL values are trending towards the experimental values as the grid is refined, but they are still under-predicted by around 5 dB on the Fine grid level. Good agreement in OASPL levels between  $70^{\circ} \le \theta \le 120^{\circ}$  is observed. Past  $130^{\circ}$  down the sideline,

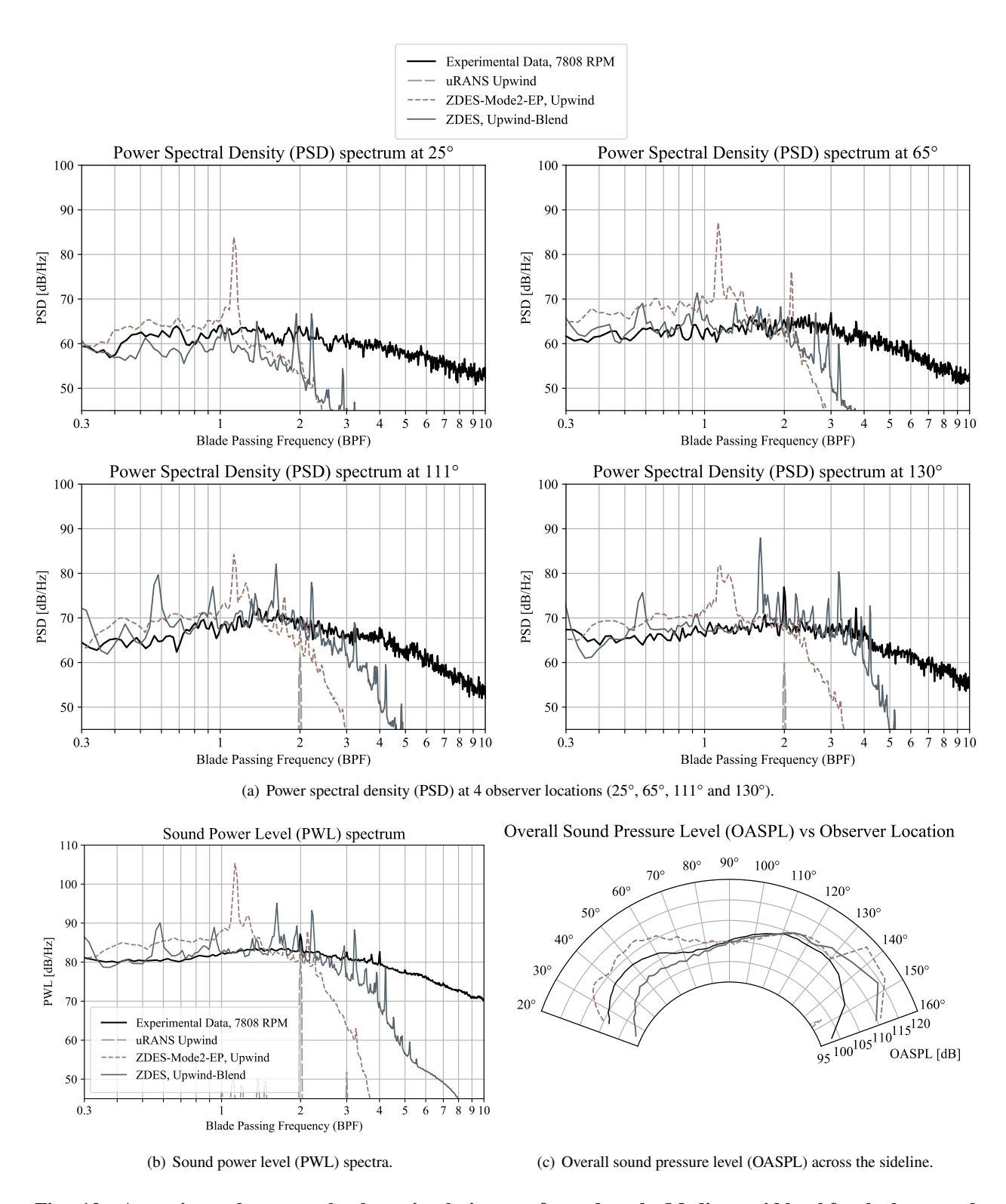
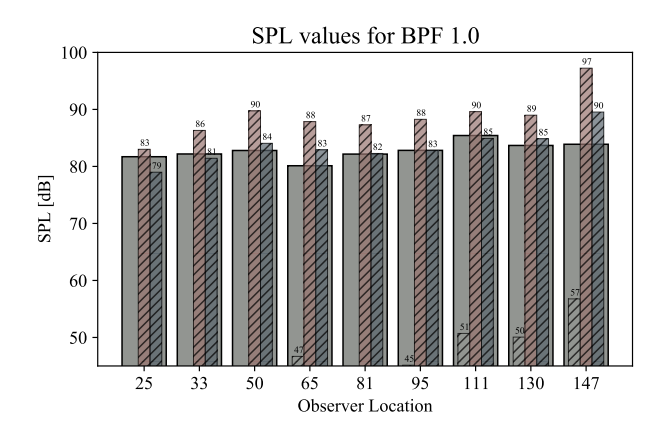


Fig. 13 Acoustic results across the three simulations performed on the Medium grid level for the low-speed operating condition compared to the experimental sideline microphone data.

the simulations over-predict the experimental OASPL values by up to 10 dB. The trend observed in the OASPL plot, showing an under-prediction of the OASPL levels in the inlet quadrant and a corresponding over-prediction towards the



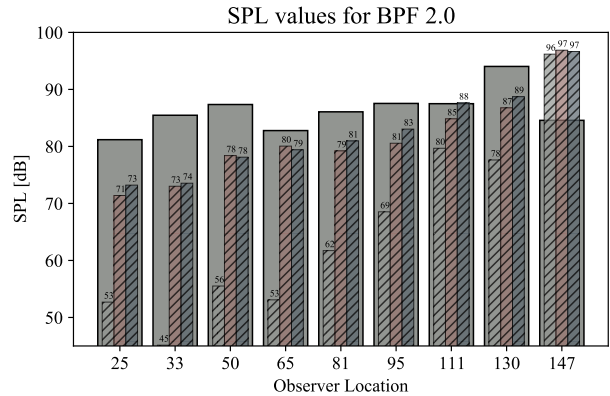


Fig. 14 SPL at several observer locations along the sideline at BPF₁ (left) and BPF₂ (right). ■ Experimental data; ℤ uRANS; ℤ ZDES-Mode2-EP, Upwind; ℤ ZDES, Upwind-Blend.

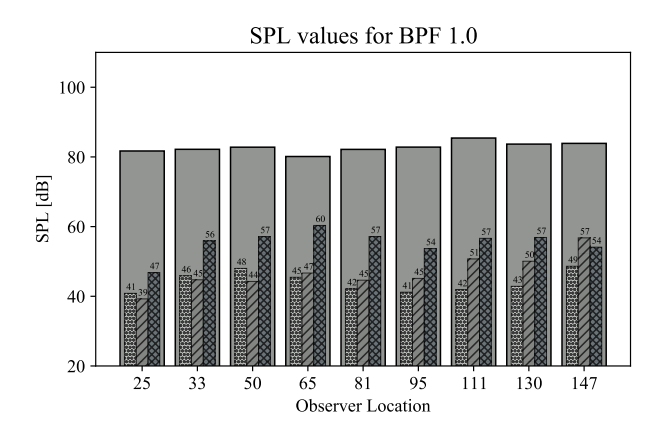
aft end of the sideline microphone array, unfortunately suggests that the good agreement in overall PWL broadband levels shown in Fig. 16(b) happen as a result of the aft angles compensating for the low high-frequency noise at the observers located in the forward arc. To understand how the OASPL levels compare with the experiment up to the frequency that the grids utilized are expected to resolve adequately, a band-limited OASPL was calculated between 1.2 kHz and 7.15 kHz (2.5BPF). Beyond 2.5BPF the number of points-per-wavelength are too low to expect these frequencies to be resolved accurately. This band-limited OASPL is shown in Fig. 17, and reveals that under-prediction of the OASPL levels in the forward arc is not just due to high-frequency content, but also due to low- and mid-frequency content not getting properly resolved under 2.5BPF. Evidence of this is also observed in Fig. 16(a) at the 25° observer location, which indicates the grid is under-resolved and would likely require more PPW to capture the mid-frequencies accurately. The mid-range region between 60° and 110° along the sideline, which for the non band-limited case showed good agreement with the experimental levels, is now over-predicted by 2 dB to 4 dB, likely due to the spurious tones observed in the PSD spectra for these observer locations.

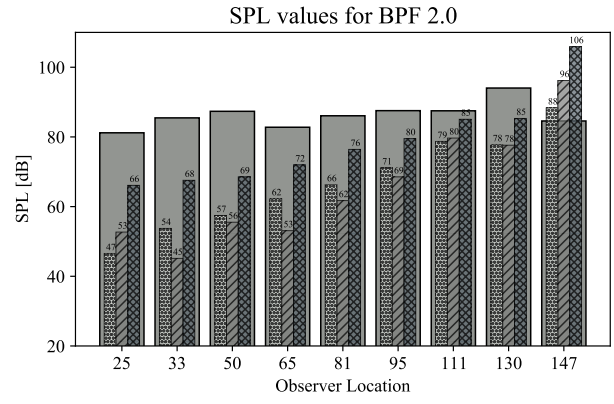
Figure 18 presents a breakdown of the inlet and exhaust contributions to the overall sound pressure levels and sound power level spectra. The experimental inlet data is taken from the a separate dataset, which avoids the exhaust contribution by shielding the sideline array from the exhaust using a physical barrier. The exhaust contribution is estimated by considering only microphones located in the exhaust quadrant relative to the nacelle exit, as suggested by Ed. Envia in a personal communication. The inlet and exhaust contributions were estimated in the simulations using the *inner-separate* FW-H surface illustrated in Fig. 7(b). Fig. 18(a) shows the inlet contributions to the OASPL for the three grid levels run using the *ZDES Upwind-Blend* approach. Large grid sensitivity is observed at sideline angles above 40°, and the inlet OASPL levels are under-predicted by around 5 dB in the inlet quadrant, which matches the differences seen in the total (inlet+exhaust) OASPL curve in the forward arc, confirming that the source for the discrepancy is indeed originating from the inlet.

Figures 18(b) and 18(c) show the inlet and exhaust PWL spectra, respectively. Here the spurious tone present at 0.4BPF can be identified as originating from the inlet, whereas the one located near BPF<sub>2</sub> is clearly visible in both spectra. The quick drop-off in broadband noise levels past BPF<sub>2</sub> previously reported at the single 25 °location is now made apparent in the PWL spectrum, and is likely the cause for the OASPL under-prediction observed in Fig. 18(a). A lack of grid resolution in the inlet could be the reason for this quick drop-off, however that would be surprising on the Fine grid level. A more convincing reason for this, in the author's perspective, is a lack of small-scale turbulent features in the interstage region (as evidenced by the PSD carpet plots in Fig. 9), which near the casing wall is likely due to the near-wall RANS mode region extending too far out and shielding the blade tip vortex region excessively. This possibility requires further investigation.

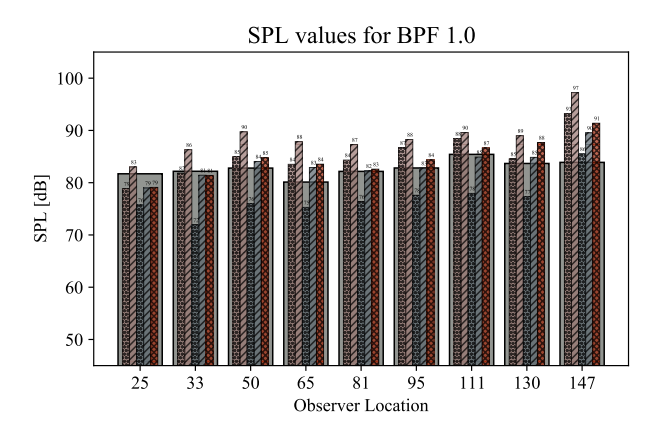
#### C. Effect of Asymmetries in Fan Blade Stagger Angle on Far-Field Acoustics

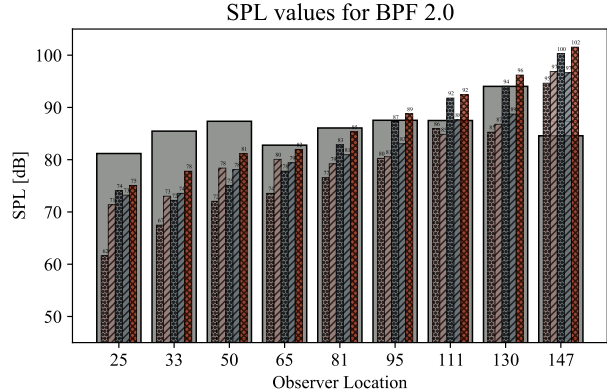
Stacked rotors, such as the R4, where each blade is individually installed in the hub, require slots in the hub that are slightly larger than the blade root such that they can easily slide into place (Envia, 2024). As a result, the blades don't lock into place uniformly when the fan is spun up, causing random deviations from the nominal blade stagger





(a) SPL at several observer locations along the sideline at BPF<sub>1</sub> (left) and BPF<sub>2</sub> (right) for the uRANS simulations on the Coarse, Medium and Fine grid levels. Experimental data; SSS Coarse grid level; Medium grid level; SSS Fine grid level.





(b) SPL at several observer locations along the sideline at BPF<sub>1</sub> (left) and BPF<sub>2</sub> (right) for the hybrid RANS/LES simulations on the Coarse, Medium and Fine grid levels. Experimental data; ZDES-Mode2-EP, Upwind, Coarse grid level; ZDES-Mode2-EP, Upwind, Medium grid level; ZDES, Upwind-Blend, Coarse grid level; ZDES, Upwind-Blend, Medium grid level; ZDES, Upwind-Blend, Fine grid level.

Fig. 15 SPL extracted at BPF<sub>1</sub> (left) and BPF<sub>2</sub> (right) for the different grid levels used in the uRANS (top) and hybrid RANS/LES (bottom) simulations at the low-speed operating condition compared with with the experimental data.

angle around the wheel. These deviation will, in turn, cause small blade-to-blade differences in the timing of their wake interactions with the OGVs, essentially detuning the rotor-stator interaction and bleeding some of the BPF-harmonic energy into shaft order tones. When the BPF<sub>1</sub> tone is cut-on and able to propagate, which for the SDT configuration only occurs at supersonic blade tip speeds, this results in multiple pure tones (MPTs) at every shaft order (sub-BPF harmonics). This effect was simulated for the high-speed regime in Gonzalez-Martino and Casalino (2018), but no such study has been published looking at the approach condition. The main difference between the two stems from the fact that because the BPF<sub>1</sub> tone is cut-off, no MPTs are generated, but an energy redistribution from tones which are cut-on, such as BPF<sub>2</sub>, should still occur.

This random deviation from the nominal blade stagger angle around the wheel was measured for the design speed to range between  $-0.25^{\circ}$  and  $0.25^{\circ}$ . Although this deviation may be different for the low-speed regime, due to a different centrifugal and aerodynamic force balance at play in the blades, these limits were used to generate a similar stagger angle deviation distribution by randomly sampling 22 samples from a uniform distribution. Fig. 19(a) shows this distribution across the blades, and Fig. 19(b) compares the asymmetric fan geometry to the original blade. Simulations with the asymmetric geometry were carried out on the Medium grid level using the *ZDES Upwind-Blend* approach, and mature solutions were generated after 15 fan revolutions.

Sound power level spectra and OASPL levels across the sideline angles for the asymmetric geometry are compared with the baseline nominal stagger angle one in Fig. 20. The OASPL levels seem to improve in the forward arc, likely

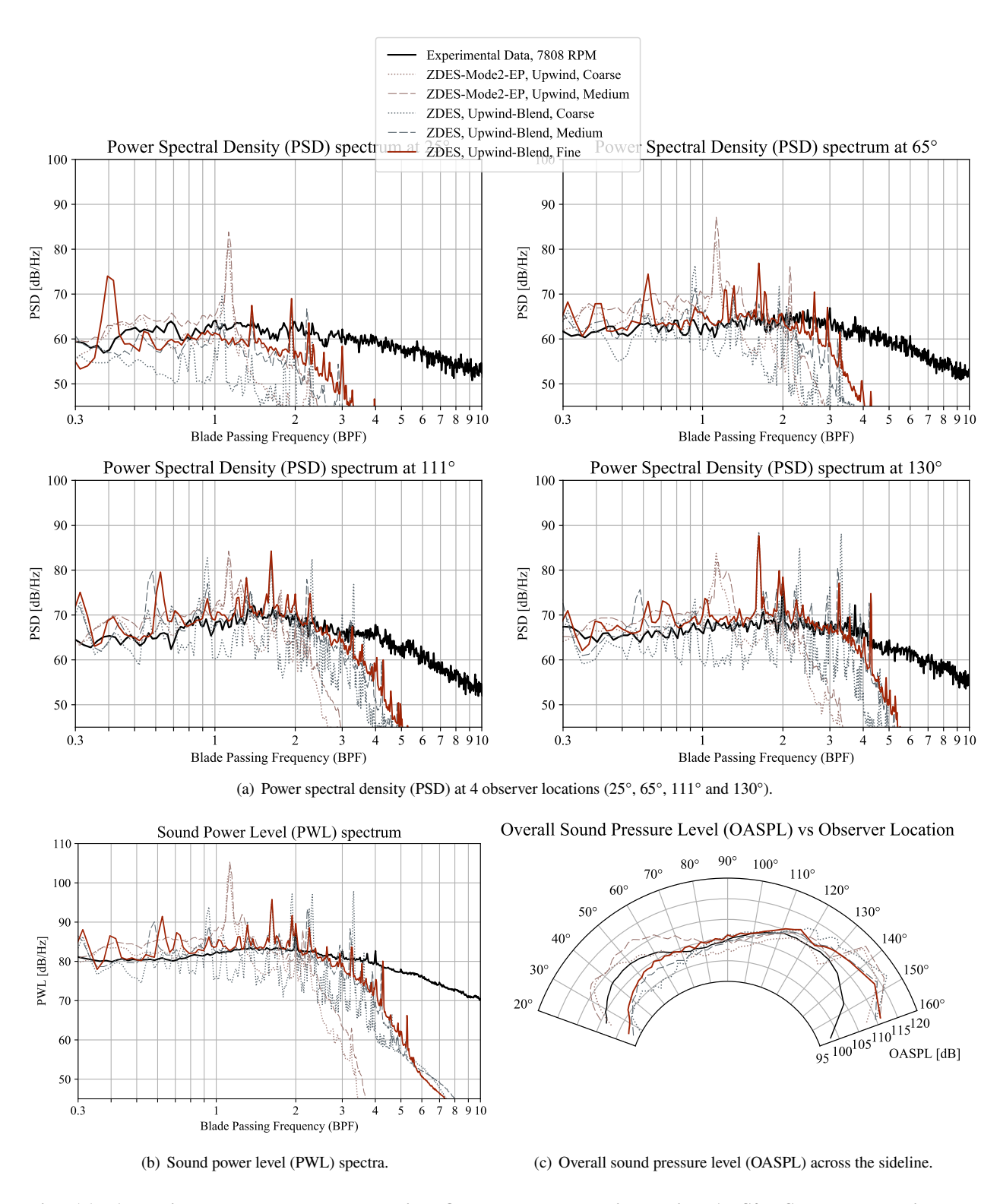
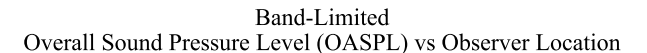


Fig. 16 Acoustic results across the three grid refinement levels used in hybrid RANS/LES approach to simulate the low-speed operating condition.

due to the over-prediction in low-frequency content now observed in the inlet PWL spectra in Fig. 20(b). Some of the energy locked in the spurious tones in the baseline configuration, especially the one located between BPF<sub>1</sub> and



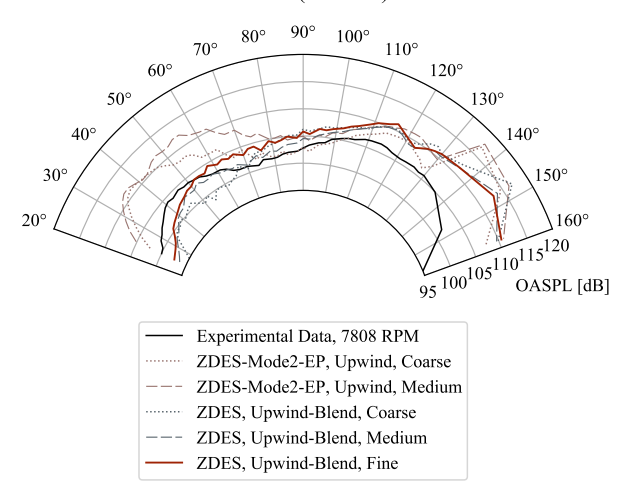


Fig. 17 Band-limited OASPL considering frequencies up to BPF<sub>2</sub>.

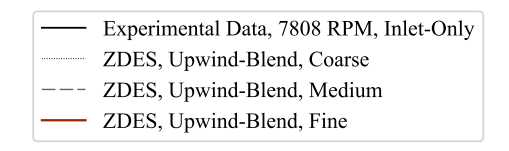
BPF<sub>2</sub>, is redistributed across the spectrum. In the exhaust, several of the spurious tones are now absent, but the energy redistribution results in an over-prediction of the broadband levels at low- and mid-frequencies. This is due to small variations in the rotor-stator interactions caused by slightly shifted wakes that now don't interact with the OGVs in exactly the same manner. This energy redistribution likely causes the appearance of several smaller tones that individually don't carry enough energy to poke out of the baseline broadband noise level. If the interstage broadband content is sufficiently well resolved, and these spurious tones caused by interactions of excessively-coherent structures in the blade wakes with the OGVs are absent, this energy redistribution mechanism would only divert energy away from tones that are cut-on, such as BPF<sub>2</sub>, and we likely wouldn't see as big of a difference between the nominal and the asymmetric geometries at the low-speed regime. Accordingly, the BPF<sub>2</sub> tone shows lower levels in the asymmetric configuration exhaust PWL spectra (Fig. 20(c)). It is curious to none also that the tone just before BPF<sub>4</sub> that was originally quiet in the baseline geometry now appears over-excited, towering over the experimental PWL by about 3 dB. Strategies to promote small-scale turbulence in the interstage region should help redistribute the energy across the spectra from the low- to mid- and high-frequencies, which is expected to improve the comparisons between the numerical simulations and the experiment.

## V. Summary

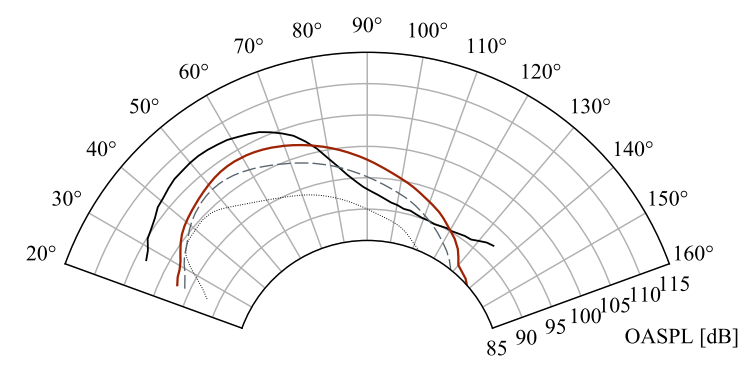
The extensive experimental dataset collected in the NASA SDT campaign is utilized in the present work to validate a sliding mesh implementation in the LAVA solver framework using both uRANS and hybrid RANS/LES approaches. An initial validation effort has already been published Fernandes et al. (2023), focusing on the overall fan stage performance metrics and validation of the interstage flow-field against hot-wire and laser Doppler velocimetry (LDV) data. This manuscript builds upon the previous one and focuses on far-field acoustic predictions at the low-speed regime.

Analysis of the interstage flow-field reveals a lack of broadband turbulent content in the mid-span and near the tip region. For the hybrid RANS/LES simulations where the RANS mode regions are defined explicitly (*ZDES Upwind-Blend*), this is likely caused by an over-shielding of the casing wall which remains in RANS mode and isn't able to properly model the small-scale turbulence that the blade tip vortex would introduce. This possibility will be investigated in future work.

Far-field acoustic propagation computations are performed using the permeable surface FW-H integral method. An extensive sensitivity study on several aspects of the FW-H approach was conducted, including effects of end-cap treatment, distance between the FW-H surface and the shear-layer in the exhaust, number of azimuthal observers over which the spectra is averaged over and sample window size, allowing for best-practices to be informed. The lack of small-scale resolved content in the interstage region appears to influence the far-field acoustics via an under-prediction of OASPL levels in the inlet and an over-prediction of up to 10 dB over the aft arc. Separation of the inlet and exhaust



## Overall Sound Pressure Level (OASPL) vs Observer Location



(a) Overall sound pressure level (OASPL) - inlet contribution.

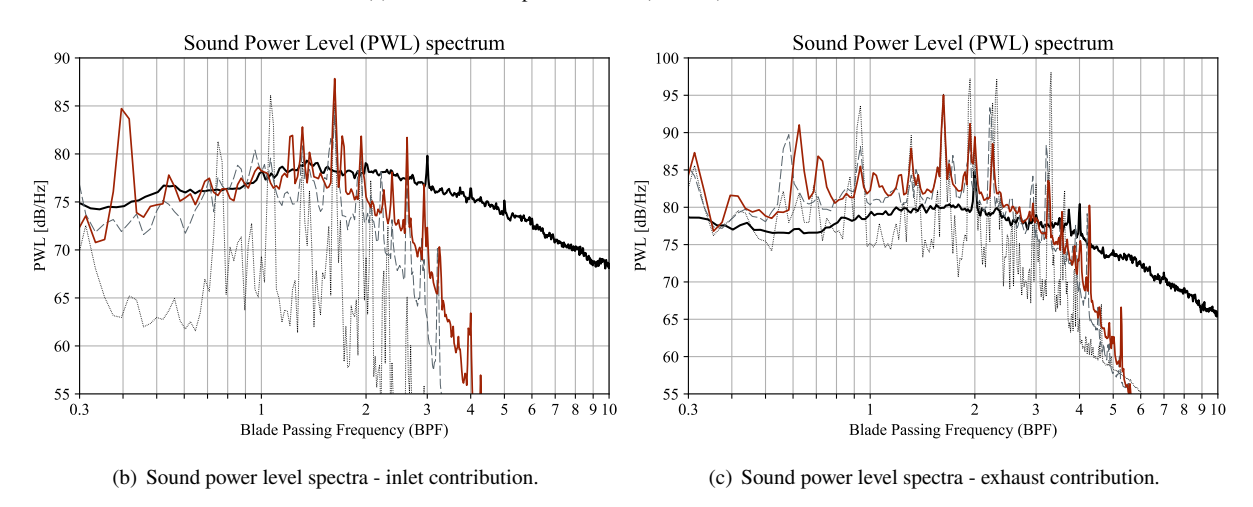
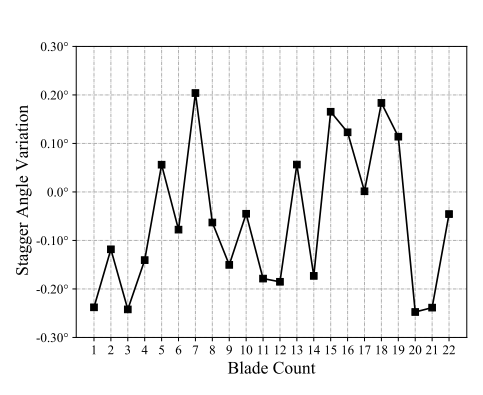


Fig. 18 Comparison and breakdown of the inlet and exhaust OASPL and PWL spectra.

PWL spectra reveals good agreement with the experimental data in the low-frequency broadband noise in the forward arc, but a quick drop-off at high-frequencies past 1.5BPF. The exhaust contribution shows an over-prediction of the low-frequency content responsible for the over-predicted OASPL levels in the aft arc. Spurious tones are visible throughout the numerical PWL spectra at seemingly random frequencies, some of which seem to be grid dependent and disappear at finer grid resolutions.

Finally, the effect of introducing random deviations to the nominal blade stagger angle around the wheel, based on the range measured in the experiment, is investigated. Several spurious tones originally observed in the baseline nominal blade stagger angle configuration appear to be absent from the asymmetric configuration, which shows a smoother PWL spectra originating from both the inlet and exhaust. The asymmetric blade spectra shows over-prediction of the low-frequency content, which ends up resulting in a fortunate improvement in the OASPL levels compared to the experiment. The detuning of the BPF2 tone is captured by this simulation, and a corresponding decrease in the BPF2 PWL is observed when the blades are stacked asymmetrically. Higher grid resolution as well as improvement of the broadband content in the interstage region is expected to improve these results in future simulations.





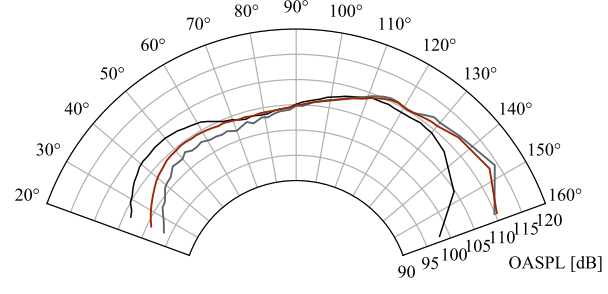
(a) Stagger angle deviation across all blades.

(b) Comparison between the original blade (yellow) and the asymmetric one (grey).

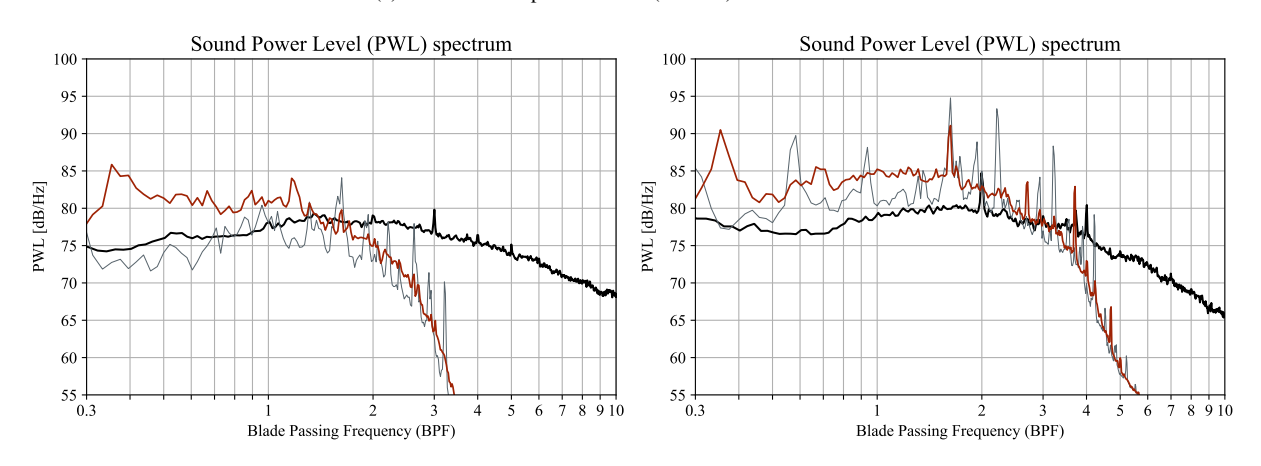
Fig. 19 Original fan blade geometry compared asymmetric geometry with deviations in the blade stagger angle.



Overall Sound Pressure Level (OASPL) vs Observer Location



(a) Overall sound pressure level (OASPL) across the sideline.



(b) Sound power level (PWL) spectra - inlet contribution.

(c) Sound power level (PWL) spectra - exhaust contribution.

Fig. 20 Far-field acoustics of asymmetric vs nominal blade geometry.

# VI. Acknowledgments

This research was funded by NASA Aeronautics Research Mission Directorate's (ARMD) Advanced Air Transport Technology (AATT) project under Advanced Air Vehicles Program (AAVP) and the Transformational Tools and Technologies (T³) project under the Transformative Aeronautics Concepts Program (TACP). Computer resources supporting this work were provided by the NASA High-End Computing (HEC) Program through the NASA Advanced Supercomputing (NAS) facility at NASA Ames Research Center (ARC). The authors would like to thank and acknowledge Dr. Edmane Envia from NASA Glenn Research Center (GRC) for providing the SDT experimental dataset and valuable insight into the interpretation of the data, Christopher Hughes (NASA GRC) for providing colored images of the original SDT test setup, and David Craig Penner and Kiran Ravikumar (NASA ARC) for their valuable feedback and review of the manuscript.

#### References

- Envia, E., "Fan Noise Reduction: An Overview," *International Journal of Aeroacoustics*, Vol. 1, No. 1, 2002a, pp. 43–64. https://doi.org/10.1260/1475472021502668, URL https://doi.org/10.1260/1475472021502668.
- Peake, N., and Parry, A. B., "Modern Challenges Facing Turbomachinery Aeroacoustics," *Annual Review of Fluid Mechanics*, Vol. 44, No. Volume 44, 2012, pp. 227–248. https://doi.org/https://doi.org/10.1146/annurev-fluid-120710-101231, URL https://www.annualreviews.org/content/journals/10.1146/annurev-fluid-120710-101231.
- Tyler, J. M., and Sofrin, T. G., "Axial Flow Compressor Noise Studies," *Pre-1964 SAE Technical Papers*, SAE International, 1962. https://doi.org/10.4271/620532, URL https://doi.org/10.4271/620532.
- Podboy, G., Krupar, M., Helland, S., and Hughes, C., "Steady and unsteady flow field measurements within a NASA 22 inch fan model," 40th AIAA Aerospace Sciences Meeting & Exhibit, Reno, NV, 2002a. https://doi.org/10.2514/6.2002-1033, URL https://arc.aiaa.org/doi/abs/10.2514/6.2002-1033.
- Hughes, C., Jeracki, R., Woodward, R., and Miller, C., "Fan Noise Source Diagnostic Test Rotor Alone Aerodynamic Performance Results," 8th AIAA/CEAS Aeroacoustics Conference & Exhibit, Breckenridge, CO, 2002. https://doi.org/10.2514/6.2002-2426, URL https://arc.aiaa.org/doi/abs/10.2514/6.2002-2426.
- Hughes, C., "Aerodynamic performance of scale-model turbofan outlet guide vanes designed for low noise," 40th AIAA Aerospace Sciences Meeting & Exhibit, Reno, NV, 2002. https://doi.org/10.2514/6.2002-374, URL https://arc.aiaa.org/doi/abs/10.2514/6.2002-374
- Heidelberg, L., "Fan Noise Source Diagnostic Test Tone Modal Structure Results," 8th AIAA/CEAS Aeroacoustics Conference & Exhibit, Breckenridge, CO, 2002. https://doi.org/10.2514/6.2002-2428, URL https://arc.aiaa.org/doi/abs/10.2514/6.2002-2428.
- Premo, J., and Joppa, P., "Fan Noise Source Diagnostic Test Wall Measured Circumferential Array Mode Results," 8th AIAA/CEAS Aeroacoustics Conference & Exhibit, Breckenridge, CO, 2002. https://doi.org/10.2514/6.2002-2429, URL https://arc.aiaa.org/doi/abs/10.2514/6.2002-2429.
- Woodward, R., Hughes, C., Jeracki, R., and Miller, C., "Fan Noise Source Diagnostic Test Far-field Acoustic Results," 8th AIAA/CEAS Aeroacoustics Conference & Exhibit, Breckenridge, CO, 2002. https://doi.org/10.2514/6.2002-2427, URL https://arc.aiaa.org/doi/abs/10.2514/6.2002-2427.
- Envia, E., "Fan Noise Source Diagnostics Test Vane Unsteady Pressure Results," 8th AIAA/CEAS Aeroacoustics Conference & Exhibit, Breckenridge, CO, 2002b. https://doi.org/10.2514/6.2002-2430, URL https://arc.aiaa.org/doi/abs/10.2514/6.2002-2430.
- Podboy, G., Krupar, M., Hughes, C., and Woodward, R., "Fan Noise Source Diagnostic Test-LDV Measured Flow Field Results," 8th AIAA/CEAS Aeroacoustics Conference & Exhibit, Breckenridge, CO, 2002b. https://doi.org/10.2514/6.2002-2431, URL https://arc.aiaa.org/doi/abs/10.2514/6.2002-2431.
- Shur, M. L., Strelets, M. K., Travin, A. K., Spalart, P. R., and Suzuki, T., "Unsteady Simulations of a Fan/Outlet-Guide-Vane System: Aerodynamics and Turbulence," *AIAA Journal*, Vol. 56, No. 6, 2018, pp. 2283–2297. https://doi.org/10.2514/1.J056645, URL https://doi.org/10.2514/1.J056645.
- Suzuki, T., Spalart, P. R., Shur, M. L., Strelets, M. K., and Travin, A. K., "Unsteady Simulations of a Fan/Outlet-Guide-Vane System: Tone–Noise Computation," *AIAA Journal*, Vol. 56, No. 9, 2018, pp. 3558–3569. https://doi.org/10.2514/1.J056646, URL https://doi.org/10.2514/1.J056646.

- Suzuki, T., Spalart, P. R., Shur, M. L., Strelets, M. K., and Travin, A. K., "Unsteady Simulations of a Fan/Outlet-Guide-Vane System: Broadband-Noise Computation," *AIAA Journal*, Vol. 57, No. 12, 2019, pp. 5168–5181. https://doi.org/10.2514/1.J058177, URL https://doi.org/10.2514/1.J058177.
- Casalino, D., Hazir, A., and Mann, A., "Turbofan Broadband Noise Prediction Using the Lattice Boltzmann Method," *AIAA Journal*, Vol. 56, No. 2, 2018, pp. 609–628. https://doi.org/10.2514/1.J055674, URL https://doi.org/10.2514/1.J055674.
- Gonzalez-Martino, I., and Casalino, D., "Fan Tonal and Broadband Noise Simulations at Transonic Operating Conditions Using Lattice-Boltzmann Methods," 2018 AIAA/CEAS Aeroacoustics Conference, Atlanta, GA, 2018. https://doi.org/10.2514/6.2018-3919, URL https://arc.aiaa.org/doi/abs/10.2514/6.2018-3919.
- Pérez Arroyo, C., Leonard, T., Sanjosé, M., Moreau, S., and Duchaine, F., "Large Eddy Simulation of a scale-model turbofan for fan noise source diagnostic," *Journal of Sound and Vibration*, Vol. 445, 2019, pp. 64–76. https://doi.org/https://doi.org/10.1016/j.jsv. 2019.01.005, URL https://www.sciencedirect.com/science/article/pii/S0022460X19300112.
- Hah, C., and Romeo, M., "LES Investigation of Wake Development in a Transonic Fan Stage for Aeroacoustic Analysis," 23rd International Symposium on Air Breathing Engines, Manchester, United Kingdom, 2017. URL https://ntrs.nasa.gov/api/citations/ 20170008798/downloads/20170008798.pdf.
- Deck, S., and Renard, N., "Towards an enhanced protection of attached boundary layers in hybrid RANS/LES methods," *Journal of Computational Physics*, Vol. 400, 2020, p. 108970. https://doi.org/10.1016/j.jcp.2019.108970, URL https://www.sciencedirect.com/science/article/pii/S0021999119306758.
- Fernandes, L. S., Housman, J. A., Kenway, G. K., Stich, G.-D., and Kiris, C. C., "Fan Noise Predictions of the NASA Source Diagnostic Test using Unsteady Simulations with LAVA Part I: Near-Field Aerodynamics and Turbulence," *AIAA SCITECH 2023 Forum*, 2023. https://doi.org/10.2514/6.2023-0793, URL https://arc.aiaa.org/doi/abs/10.2514/6.2023-0793.
- di Francescantonio, P., "A NEW BOUNDARY INTEGRAL FORMULATION FOR THE PREDICTION OF SOUND RADIATION," *Journal of Sound and Vibration*, Vol. 202, No. 4, 1997, pp. 491–509. https://doi.org/https://doi.org/10.1006/jsvi.1996.0843, URL https://www.sciencedirect.com/science/article/pii/S0022460X96908433.
- Lockard, D., "A Comparison of Ffowcs Williams-Hawkings Solvers for Airframe Noise Applications," 8th AIAA/CEAS Aeroacoustics Conference & Conference
- Kiris, C. C., Housman, J. A., Barad, M. F., Brehm, C., Sozer, E., and Moini-Yekta, S., "Computational framework for Launch, Ascent, and Vehicle Aerodynamics (LAVA)," *Aerospace Science and Technology*, Vol. 55, 2016, pp. 189–219. https://doi.org/10.1016/j. ast.2016.05.008, URL https://www.sciencedirect.com/science/article/pii/S127096381630178X.
- Vinokur, M., "Conservation equations of gasdynamics in curvilinear coordinate systems," *Journal of Computational Physics*, Vol. 14, No. 2, 1974, pp. 105–125. https://doi.org/10.1016/0021-9991(74)90008-4, URL https://www.sciencedirect.com/science/article/pii/0021999174900084.
- Housman, J. A., and Kiris, C. C., "Structured Overlapping Grid Simulations of Contra-Rotating Open Rotor Noise," 54th AIAA Aerospace Sciences Meeting, San Diego, CA, 2016. https://doi.org/10.2514/6.2016-0814, URL https://arc.aiaa.org/doi/abs/10.2514/6.2016-0814.
- Steger, J. L., and Benek, J. A., "On the use of composite grid schemes in computational aerodynamics," *Computer Methods in Applied Mechanics and Engineering*, Vol. 64, No. 1, 1987, pp. 301–320. https://doi.org/10.1016/0045-7825(87)90045-4, URL https://www.sciencedirect.com/science/article/pii/0045782587900454.
- Spalart, P., and Allmaras, S., "A one-equation turbulence model for aerodynamic flows," 30th Aerospace Sciences Meeting & Exhibit, Reno, NV, 1992. https://doi.org/10.2514/6.1992-439, URL https://arc.aiaa.org/doi/abs/10.2514/6.1992-439.
- Spalart, P. R., Deck, S., Shur, M. L., Squires, K. D., Strelets, M. K., and Travin, A., "A New Version of Detached-eddy Simulation, Resistant to Ambiguous Grid Densities," *Theoretical and Computational Fluid Dynamics*, Vol. 20, No. 3, 2006, p. 181. https://doi.org/10.1007/s00162-006-0015-0, URL https://doi.org/10.1007/s00162-006-0015-0.
- Deck, S., "Recent improvements in the Zonal Detached Eddy Simulation (ZDES) formulation," *Theoretical and Computational Fluid Dynamics*, Vol. 26, No. 6, 2012, pp. 523–550. https://doi.org/10.1007/s00162-011-0240-z, URL https://doi.org/10.1007/s00162-011-0240-z.
- Dumlupinar, E., Housman, J. A., Kenway, G. K., and Kiris, C. C., "Unsteady RANS and Scale Resolving Simulations of Open Rotor Noise," AIAA SciTech 2023 Forum, 2023. https://doi.org/10.2514/6.2023-0028, URL https://arc.aiaa.org/doi/abs/10.2514/6.2023-0028.

- Housman, J. A., Kiris, C. C., and Hafez, M. M., "Time-Derivative Preconditioning Methods for Multicomponent Flows—Part I: Riemann Problems," *Journal of Applied Mechanics*, Vol. 76, No. 2, 2009a. https://doi.org/10.1115/1.3072905, URL https://doi.org/10.1115/1.3072905, 021210.
- Housman, J. A., Kiris, C. C., and Hafez, M. M., "Time-Derivative Preconditioning Methods for Multicomponent Flows—Part II: Two-Dimensional Applications," *Journal of Applied Mechanics*, Vol. 76, No. 3, 2009b. https://doi.org/10.1115/1.3086592, URL https://doi.org/10.1115/1.3086592, 031013.
- Koren, B., "A robust upwind discretization method for advection, diffusion and source terms," *Numerical Methods for Advection-Diffusion Problems*, edited by C. Vreugdenhil and B. Koren, Vieweg, Germany, 1993.
- Stich, G.-D., S. Fernandes, L., Housman, J. A., Kenway, G. K., and Kiris, C. C., "Validation of Actuator Disk, Actuator Line and Sliding Mesh Methods within the LAVA solver," *11th International Conference on Computational Fluid Dynamics (ICCFD)*, 2022. URL https://www.iccfd.org/iccfd11/assets/pdf/papers/ICCFD11\_Paper-0903.pdf.
- Browne, O. M., Housman, J. A., Kenway, G. K., Ghate, A. S., and Kiris, C. C., "A Hybrid RANS-LES Perspective for the High Lift Common Research Model Using LAVA," *AIAA Aviation 2022 Forum*, Chicago, IL, 2022. https://doi.org/10.2514/6.2022-3523, URL https://arc.aiaa.org/doi/abs/10.2514/6.2022-3523.
- Kiris, C. C., Ghate, A. S., Duensing, J. C., Browne, O. M., Housman, J. A., Stich, G.-D., Kenway, G., Fernandes, L. S., and Machado, L. M., "High-Lift Common Research Model: RANS, HRLES, and WMLES perspectives for CLmax prediction using LAVA," AIAA SCITECH 2022 Forum, 2022. https://doi.org/10.2514/6.2022-1554, URL https://arc.aiaa.org/doi/abs/10.2514/6.2022-1554.
- Brown, C. A., and Schifer, N. A., "Low Frequency Noise Contamination in Fan Model Testing," *Turbo Expo: Power for Land, Sea, and Air*, Vol. Volume 6: Turbomachinery, Parts A, B, and C, 2008. https://doi.org/10.1115/GT2008-50850, URL https://doi.org/10.1115/GT2008-50850.
- Shur, M. L., Spalart, P. R., and Strelets, M. K., "Noise Prediction for Increasingly Complex Jets. Part I: Methods and Tests," *International Journal of Aeroacoustics*, Vol. 4, No. 3, 2005, pp. 213–245. https://doi.org/10.1260/1475472054771376, URL https://doi.org/10.1260/1475472054771376.
- Mendez, S., Shoeybi, M., Lele, S. K., and Moin, P., "On the Use of the Ffowcs Williams-Hawkings Equation to Predict Far-Field Jet Noise from Large-Eddy Simulations," *International Journal of Aeroacoustics*, Vol. 12, No. 1-2, 2013, pp. 1–20. https://doi.org/10.1260/1475-472X.12.1-2.1, URL https://doi.org/10.1260/1475-472X.12.1-2.1.
- Envia, E., personal communication, 2024.